ELSEVIER

Surface Science 421 (1999) 205–236

surface science

X-ray photoelectron diffraction study of thin Cu films grown on clean Ru(0001) and O-precovered Ru(0001)

S.D. Ruebush [a], R.E. Couch [a], S. Thevuthasan [b], C.S. Fadley [a,c,*]

[a] *University of California–Davis, Davis, CA 95616, USA*
[b] *Molecular Science Research Center, Pacific Northwest Laboratory, Richland, WA 99352, USA*
[c] *Material Sciences Division, Lawrence Berkeley National Laboratory, Berkeley, CA 94720, USA*

Received 10 March 1998; accepted for publication 15 September 1998

Abstract

We have studied the epitaxial growth modes and near-surface interlayer relaxation of thin Cu films on Ru(0001) using X-ray photoelectron diffraction (XPD), measuring experimental Cu $2p_{3/2}$ ($E_{kin}=556$ eV) and Ru 3d ($E_{kin}=1206$ eV) intensities over one-third of the nearly full 2π solid angle above the surface for Cu coverages from submonolayer up to 40 monolayers. Reference Cu $2p_{3/2}$ data for a clean Cu(111) surface have also been obtained from Naumović et al. and in our laboratory. These data have been compared to single scattering cluster (SSC) and more accurate multiple scattering cluster (MSC) calculations via a sum of five *R*-factors to derive precise structural information. MSC calculations are found to give a more accurate description for layers of ≥ 4 ML thickness, and comparisons of experiment and theory are also improved by allowing more accurately for the effective degree of angular averaging involved. Calculations for thicker layers are also found to converge by ~ 5 ML. Our analysis indicates that the first Cu layer grows pseudomorphically on Ru(0001), in agreement with prior studies. An *R*-factor analysis comparing MSC and SSC calculations to experimental results further indicates that the Cu–Ru interlayer spacing at 1 monolayer (ML) is about 2.15 Å, in excellent agreement with prior low-energy ion scattering (LEIS) and low-energy electron diffraction (LEED) experimental studies, as well as with prior linearized augmented plane-wave (LAPW) calculations. At higher coverages, comparison of our data to SSC and MSC calculations for various atomic clusters indicates that the short-range structure is fcc Cu(111)-like, but with significant interlayer contraction which persists up to ≥ 5 ML coverage. Prior STM work by Behm et al. has shown a series of misfit dislocation structures in the top layer of the Cu film at higher coverages from 2 to 4 ML. Our data indicate that these misfit dislocation structures thread to the Cu/Ru interface rather than occurring only in the top Cu layer or layers. An *R*-factor comparison of the more accurate MSC calculations to experiment also indicates that the ratio of the Cu–Cu interlayer distance ($d_\perp$) to the Cu–Cu in-plane nearest-neighbor distance ($d_\parallel$), $d_\perp/d_\parallel=0.729\pm0.034$ at 2 ML, and reaches 0.777 ± 0.020 by 25 ML. For reference, the bulk value is $d_\perp/d_\parallel=0.816$, and the analysis of experimental data for Cu(111) yields 0.801 ± 0.035, in good agreement with this value and prior LEED studies. This analysis shows that there is significant interlayer contraction for very thin Cu layers, and that it persists (at least in the top few layers, to which XPD is the most sensitive) for longer than would be expected on the basis of a prior theoretical analysis using the 2D Frenkel–Kontorova model by Hamilton and Foiles, as used to estimate $d_\perp/d_\parallel$ via either a constant atomic-volume assumption or elasticity theory. In addition, the Cu overlayer grows in two possible orientations rotated by 180° on the Ru(0001) surface, with a preference towards one of the two possible orientations at certain coverages. Finally, we have investigated the effect of oxygen preadsorbed on the Ru(0001) surface on the growth of the Cu overlayer. For this case, we find that all of the oxygen floats on top of the Cu in a highly disordered configuration, and that the oxygen promotes multilayer or island growth relative to growth on the clean Ru surface up to at least 3 ML coverage, rather than acting as a surfactant promoting smoother growth.

Keywords: Copper; Epitaxy; Low energy electron diffraction; Oxygen; Ruthenium; Single-crystal epitaxy; Surface structure, morphology, roughness, and topography; X-ray photoelectron diffraction

* Corresponding author. Fax: +1 530 7524717.

0039-6028/99/$ – see front matter
PII: S0039-6028(98)00741-9

1. Introduction

The growth of thin epitaxial metal films on metal substrates has attracted much interest recently due to the unusual catalytic, electronic or magnetic properties such systems may exhibit [1]. The atomic-scale structure of these systems plays an important role in their physical and chemical properties. Heteroepitaxial metal-on-metal systems are of particular interest because the misfit between the substrate lattice geometry and the overlayer bulk geometry causes strain in the overlayer, which in turn can lead to altered growth modes and expansions or contractions of interatomic or interlayer distances in the overlayer [1]. Such heteroepitaxial systems thus offer the possibility of producing novel atomic structures which may exhibit unique properties. An understanding of how the substrate lattice geometry influences overlayer growth and structure is thus vital to the development of nanostructured materials with new and useful properties. The heteroepitaxial system Cu/Ru(0001) has become a model system for such strained overlayer systems due to the several interesting structural transformations which occur in the Cu overlayer as the film thickness is increased, particularly in the range from 1 monolayer (ML) to 4 ML [2–5]. These structural transitions are driven by a balance between the misfit energy and the strain energy of the Cu overlayer [6]. The misfit is such that the lattice constant of fcc Cu(111) which ultimately grows in thicker layers is 5.5% smaller than that of the hcp Ru(0001) substrate.

Early studies of the Cu/Ru(0001) system using Auger electron spectroscopy (AES), low-energy electron diffraction (LEED), thermal desorption spectroscopy (TDS) and work-function measurements concluded that the growth was Stranski–Krastonov in character [7–12]. However, more recent studies using scanning tunneling microscopy (STM) have provided a much more detailed and complex picture, and revealed that the Cu grows via a series of misfit-dislocation structures [2–5]. These dislocation structures have also been predicted recently in a theoretical study by Hamilton and Foiles [6], who used a 2D Frenkel–Kontorova model to determine the minimum energy configuration for thin Cu films grown on Ru(0001), and obtained results which were in basic agreement with the STM structures. The STM studies [2–5] concluded that the first Cu layer expands by 5.5% from the bulk Cu(111) lateral spacing to grow pseudomorphically, with the Cu atoms occupying the three-fold hollow sites of the Ru(0001) surface. At 2 ML, a striped dislocation pattern was observed in which the layer was assumed to contract uniaxially from the pseudomorphic configuration via misfit dislocations. At 3 ML, the Cu surface layer contracts along three directions from the pseudomorphic configuration to form a complex network of triangular structures, but still with an overall lateral expansion by about 2% from the bulk fcc Cu(111) configuration. At 4 ML, a large-scale incommensurate lateral superlattice or moiré pattern was observed. At coverages of 4 ML and higher, the Cu overlayer is thought to relax almost fully to a bulk fcc Cu(111) lateral spacing [2–6], but two separate quantitative analyses of the 4 ML atomic-resolution STM moiré pattern [5,13] still indicate a 0.6% lateral expansion relative to bulk Cu(111). These STM studies [2–5] also concluded that, at 300 K, the growth is layer-by-layer up to at least 2 ML, but that 3D islands and a distribution of island heights peaked around the nominal thickness form at higher coverages. Detailed measurements of the distributions of different layer thicknesses for different coverages and thermal treatments have also been made [5]. A very recent LEED study has permitted the additional conclusion that the structural data derived on a local scale by STM are representative of the entire surface as analyzed by LEED, and also permitted a more exact determination of both lattice periodicities and lattice rotations [14,15]. However, from STM it is not possible to determine whether the misfit dislocation structures thread to the Cu–Ru interface or occur only in the top Cu layer or layers. Nor does STM permit a determination of the vertical spacing between adjacent Cu layers. We have thus applied X-ray photoelectron diffraction (XPD) to both of these questions, with a preliminary account of this work having appeared previously [16].

Other studies have found that the growth of thin epitaxial metal films on metal substrates may be strongly affected by contaminants such as preadsorption of oxygen on the original substrate surface [17,18]. In certain cases, such preadsorption can lead to smoother overlayer growth through what has been termed a surfactant role [19–21]. These studies have suggested that when oxygen is preadsorbed on the Ru(0001) substrate, the growth mode of the Cu overlayer may be changed from multilayer and/or 3D islands to a more 2D layer-by-layer growth mode, thus achieving smoother film morphologies [19–21]. For example, work-function studies [20,21] have reported oscillations in the work function starting at about 3 ML when Cu was grown at $\sim$125°C on a Ru(0001) surface which had been precovered with O up to 0.4 ML coverage. Smoluchowski dipoles at island step edges tend to lower the work function, and thus these work-function oscillations were attributed to a changing Cu step-edge length, which became large during nucleation of many small 2D Cu islands, grew smaller as the islands grew larger, and finally coalesced near the completion of a layer. Schmidt et al. [21] further concluded that when oxygen is preadsorbed on Ru(0001), Cu grows layer-by-layer up to as many as 50 ML, and that 85% of the oxygen floats on the Cu surface during the film growth, while the rest remains at the Cu/Ru interface. A more recent low-energy ion scattering (LEIS) study concluded that 70% of the oxygen floats on the Cu surface, and in addition that the oxygen layer is disordered on the Cu surface [22]. We have thus explored these questions using XPD.

X-ray photoelectron diffraction (XPD) is an excellent tool with which to derive additional information about the Cu/Ru(0001) system [23–26]. The strong forward scattering effect along internuclear axes for core-level emission at high energies ($E_{kin} \geq 500$ eV) permits the quick identification of buried species and determination of the local structural environment around an emitting atom, and thus can provide information about epitaxial growth modes and lattice expansions or contractions. Since diffraction patterns for the overlayer element as well as the substrate element can be measured simultaneously, information about the preferred orientation of the overlayer relative to the substrate can also be determined [23–26]. XPD is also a probe of short-range atomic structure, such that long-range order is not required to derive structural information. Finally, more detailed structural information can be determined by comparing experimental data to single-scattering cluster (SSC) and more accurate multiple-scattering cluster (MSC) diffraction calculations via *R*-factors [27–30].

2. Experiment

The Ru(0001) surface was prepared by mechanically polishing a Ru single crystal, 0.5 in in diameter, using a final abrasive of 0.05μ alumina. The polished crystal was oriented by Laue back reflection and the surface was found to be within 0.5° of the (0001) orientation. The polished and oriented Ru(0001) crystal was cleaned further in a UHV chamber attached to the photoelectron spectrometer, in which the base pressure was near 5×10^{-11} Torr. The in situ cleaning consisted of mild Ar^+ ion bombardment (5.5×10^{-5} Torr, 800 eV, 30 mA) followed by several oxygen and heat treatments in which the Ru sample was heated to $\sim$800°C in an oxygen atmosphere of 3×10^{-7} Torr for $\sim$5 min and then briefly vacuum-annealed at $\sim$1400°C. Surface cleanliness was verified by X-ray photoelectron spectroscopy (XPS) [23–26]. Typical oxygen impurity levels were $\leq$0.05 ML. Carbon impurity levels were more difficult to estimate due to the overlap of the C 1s and Ru $3d_{3/2}$ levels, but cross comparisons of the intensities of the Ru $3d_{3/2}$ and Ru $3d_{5/2}$ peaks in different stages of cleanliness permit the estimation that carbon was present at levels of $\leq$0.1 ML. The presence of a well-ordered Ru(0001) surface was verified by a sharp hexagonal LEED pattern. In order to ensure that the Ru(0001) surface remained clean and well ordered, the same cycle of oxygen and heat treatments, as well as XPS and LEED measurements, were performed before each Cu deposition.

The thin Cu films were made by evaporating Cu onto the Ru substrate from a resistively heated W

wire wrapped with high-purity (99.998%) Cu wire. The Ru substrate temperature during deposition was ~600°C for Cu coverages of ≤3 ML and ~300°C for Cu coverages of ≥5 ML, with the lower temperature being used for thicker layers to suppress evaporation effects [7,8]. However, a 4.2 ML film of intermediate coverage was obtained by initially depositing Cu at 300°C to a coverage of 7.7 ML and then briefly heating to 600°C to yield the final lower coverage via evaporation. After heating, XPS measurements indicated a Cu coverage of 4.2 ML. These preparation conditions thus correspond to those used in prior studies [2–12], although we note that a very recent STM study has explored the detailed temperature dependence, and concluded that, for layers above 2 ML, higher substrate temperatures promote more multilayer/3D island growth [5]. The overall Cu coverage was determined in two independent ways, via measurements of total deposition using a quartz crystal monitor (QCM; Leybold-Inficon Model 751-001-G1) and angular-dependent XPS [22]. The QCM values should represent upper limits of coverage, with the values possibly being decreased by subsequent evaporation and/or 3D island formation of some of the Cu, especially for thicker films. Details concerning the quantitative XPS analysis appear elsewhere [13], but they involved determining a Cu $2p_{3/2}$/Ru 3d intensity ratio which was averaged over the azimuthal angle and spline-smoothed over polar angle, and then applying standard surface analysis formulae. The deposition rates as measured by the QCM were between 0.4 and 1.3 ML min^{-1}. The coverages determined from QCM and XPS measurements are shown in Table 1, and the values obtained from the two different measurements are in general in good agreement with each other. The XPS values are in any case viewed as a more accurate measure of the actual final coverages on the surface. For a very thick Cu overlayer, Cu was deposited until the substrate Ru 3d XPS signal could no longer be seen due to electron inelastic attenuation through the Cu overlayer, thus indicating an effectively infinitely thick Cu film. Based on the deposition rate as measured by the QCM, the thickness of this very thick Cu overlayer was ~25.2 ML. For Cu grown on O-precovered Ru(0001), the clean Ru surface was first exposed to 90 L of oxygen until a saturation coverage of 0.5 ML was reached. This led to a well-ordered $p(2\times1)$-O/Ru(0001) structure as confirmed by LEED. Copper was then evaporated as for Cu/clean Ru(0001), but at a substrate temperature of ~125°C in order to correspond to prior work on this system [19–21]. However, a 3.7 ML film was prepared by briefly annealing a 6.5 ML Cu film at 325°C in order to obtain a $(2\sqrt{3}\times4\sqrt{3})R30^\circ$ LEED structure as seen in Ref. [20]. After annealing, XPS indicated a coverage of 3.7 ML. Here we have calculated the coverage in a way which assumes an overlayer of uniform thickness which covers the entire substrate surface. Thus, we believe that the apparent reduction in coverage upon annealing to 325°C is due to a change in morphology in which part of the Ru surface may have become uncovered rather than to the desorption of any Cu. In Table 2 we present the Cu coverages as determined from both QCM and XPS measurements for the O-precovered Ru surface.

Table 1
Cu coverages as determined by QCM and XPS for Cu/Ru(0001)

Cu (ML) by QCM	Cu (ML) by XPS
0.24	0.38
1.8	1.1
2.2	2.0
3.0	2.9
[a]	4.2
5.9	4.9
[b]	6.5
9.0	8.0
25.2	∞

[a]Sample was initially 7.7 ML and was annealed at 600°C to desorb Cu until a nominal coverage of ~4 ML was reached. Therefore, no QCM data is available for this coverage. The coverage after annealing was 4.2 ML according to XPS.
[b]No QCM data taken at this coverage.

The experiments were performed with a Hewlett-Packard 5950A photoelectron spectrometer which was specially modified for ultrahigh vacuum XPD studies [23–26]. The base pressure of the experimental chamber was 5×10^{-11} Torr. Al Kα radia-

Table 2
Cu coverages determined by QCM and XPS for Cu/O/Ru(0001)

Cu (ML) by QCM	Cu (ML) by XPS
0.56	0.60
1.8	1.1
1.4	2.2
2.16	3.2
[a]	3.7
3.4	4.8
5.7	6.5
6.1	8.0
30.5	∞

[a]Sample was initially 6.5 ML and was annealed at 325°C in order to obtain a $(2\sqrt{3}\times 4\sqrt{3})$R30° LEED structure as seen in Ref. [18]. The Cu coverage after annealing was 3.7 ML according to XPS.

tion ($h\nu = 1486.6$ eV) was used to excite Cu $2p_{3/2}$ ($E_{kin} = 556$ eV), Ru 3d ($E_{kin} = 1206$ eV) and O 1s ($E_{kin} = 955$ eV) photoelectrons. A special non-monochromatized X-ray tube was added to this system, and it yielded about three times higher data acquisition rates than the normal monochromatized source [31]. The experimental geometry is shown in Fig. 1. The angle between photon incidence and electron exit was fixed at 72°. The intensities of all peaks were measured over one-third of the nearly full 2π solid angle above the sample surface, thus exploiting the three-fold symmetry of the Cu/Ru system to reduce scan time. However, the three-fold symmetry was verified for all overlayers studied by performing full 360° azimuthal scans at selected polar angles. Thus, both the polar (θ) and azimuthal (ϕ) emission angles were varied, with θ being measured from the sample surface and ϕ from the [001] direction lying in the Ru surface. Scanning was over the ranges $6° \le \theta \le 90°$ and $0° \le \phi \le 120°$, with full-hemisphere intensity patterns then being generated by three-fold repetition of each set of data. The step size in θ was 2°. The step size in ϕ was initially 2° at $\theta = 6°$, and was increased as θ increased so that the data density in the solid angle would remain roughly constant over the full data set above the sample surface. The formula used to adjust the size of the ϕ step was

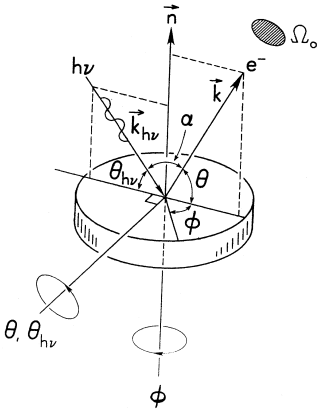

Fig. 1. Illustration of the basic experimental geometry in the XPD experiment. The polar angle ϕ of electron emission is measured from the surface. The angle α between the incoming radiation and the outgoing wave vector was fixed for these experiments at 72°.

$$\Delta\phi = \Delta\phi_{init.}\frac{\sin\left(\frac{90° - \theta_{init.}}{2}\right)}{\sin\left(\frac{90° - \theta}{2}\right)}, \quad (1)$$

where $\Delta\phi_{init.} = 2°$ and $\theta_{init.} = 6°$ for our data.

Because the limit for thicker coverages is a Cu(111) epitaxial layer, we also measured the Al Kα-excited Cu $2p_{3/2}$ XPD pattern at 556 eV from a bulk Cu(111) specimen. This was mechanically polished, chemically polished, and oriented (to within 0.5° of (111)) and cleaned in situ using standard methods. Additional Cu $2p_{3/2}$ XPD patterns at slightly different kinetic energies of 321 eV (Mg Kα) and 808 eV (Si Kα) were also obtained from the data of Naumović and Osterwalder [32,33]. These data provide an important reference for the ideal Cu(111) structure, to which we will return later.

All of the XPD intensities from our experiments have been normalized so as to include only the diffraction features. The normalized intensity $\chi(\boldsymbol{k})$ is defined as $\chi(\boldsymbol{k}) = [I(\boldsymbol{k}) - I_0(\boldsymbol{k})]/I_0(\boldsymbol{k})$, where $I(\boldsymbol{k})$ is the measured photoelectron intensity, $I_0(\boldsymbol{k})$ is the photoelectron intensity in the absence of any scattering, and $\boldsymbol{k}$ is the photoelectron wave vector. In presenting and analyzing the experimental data,

we have estimated $I_0(\boldsymbol{k})$ by applying a spline-smoothing routine [34] to $I(\boldsymbol{k})$ so that the diffraction features have been smoothed out. In this procedure, the data were first azimuthally averaged, so that

$$\bar{I}(\theta_i) = \frac{1}{n} \sum_{j=1}^{n} I(\theta_i, \phi_j), \tag{2}$$

where n is the number of ϕ_j steps at each θ_i. The spline function was then fit to $\bar{I}(\theta_i)$ to derive $I_0(\boldsymbol{k})$. The smoothing factor of this spline fit was adjusted so that it removed only a smooth background following the instrumental variation of intensity with polar angle, which in general shows an approximate $\sin\theta$ variation. Details of this procedure appear elsewhere [13], and it is very useful in amplifying weaker total-intensity features for lower takeoff angles which nonetheless contain considerable structural information.

3. Results and discussion

3.1. Cu grown on clean Ru(0001)

3.1.1. XPD: experimental results

In Fig. 2a–i, we present the measured XPD patterns for the Cu $2p_{3/2}$ peak at nine different Cu coverages from 0.4 to 25 ML. In Fig. 2j and k, we show the same XPD pattern from a bulk Cu(111) crystal: in Fig. 2k the raw data with three-fold symmetry are shown, and in Fig. 2j the same data which has been made six-fold via a 60° rotation and addition of two patterns is shown. In addition, for reference to the substrate, we show in Fig. 2l the measured XPD pattern for the Ru 3d peak for a clean Ru sample. The low-index direction $[2\bar{1}\bar{1}]$ for Cu(111) is along the 90° azimuth in Fig. 2k, and the low-index direction [210] for Ru is along the 30° azimuth in Fig. 2l. Note that the hcp Ru(0001) pattern is inherently six-fold, whereas that of fcc Cu(111) is three-fold. This is due to the ABABAB… stacking in the hcp lattice, which inverts its three-fold local-scattering symmetry pattern from one monatomic step to another. In contrast, the ABCABCABC… stacking in fcc does not invert its local symmetry across a monatomic step. The XPD pattern for Ru 3d does not change significantly as thicker Cu layers are grown, and so we do not show the XPD patterns for Ru 3d at each Cu coverage.

As a measure of the degree of diffraction present for these XPD patterns, we show in Fig. 3a the relative anisotropy, i.e. $[I_{\max}(\theta) - I_{\min}(\theta)]/I_{\max}(\theta) = \Delta I(\theta)/I_{\max}(\theta)$, as a function of polar angle and coverage: here, this is computed for each azimuthal scan. The absolute anisotropies range from about 5% at the lowest points on the curves up to about 30% at the highest points on the curves. A scale is included in each panel in Fig. 3 to indicate the relative amounts of anisotropy versus polar angle. Comparing Fig. 2a and b and Fig. 3a for 0.4 and 1.1 ML, we see that the peak in anisotropy near 15° is due to the pronounced first-order diffraction rings [24] originating in electrons scattered from nearest-neighbor and next-nearest neighbor atoms in the surface plane of the hexagonal array of pseudomorphic Cu atoms, as we will confirm with a more detailed theoretical analysis of the XPD patterns below. Note also that the essential identity of Fig. 2a and b and of the anisotropy curves for 0.4 and 1.1 ML in Fig. 3a immediately implies that the Cu atoms at 0.4 ML are clustering together into pseudomorphic islands which are large compared to the short-range order sensing diameter of XPD of $\sim$20–30 Å. The peak in anisotropy at 0.4 and 1.1 ML near $\theta = 15°$ is thus due to the variation in intensity caused by the diffraction rings at low θ. The anisotropy at higher angles is nearly zero for these two lowest coverages and is due mainly to noise, although a weak six-fold pattern is seen for the 1.1 ML case in Fig. 2b. For thicker Cu layers, polar angles associated with nearest-neighbor interatomic directions should have the largest anisotropies since such directions imply strong forward scattering and a rapid variation in intensity. To provide some idea of where such directions occur, we show in Fig. 4 an atomic model for Cu(111) with a top view of the Cu(111) surface and also a cross-section through the $[2\bar{1}\bar{1}]$ direction. The low-index directions and most prominent forward scattering directions are also indicated in Fig. 4b. Comparison of these forward scattering directions to the diffraction patterns and the exper-

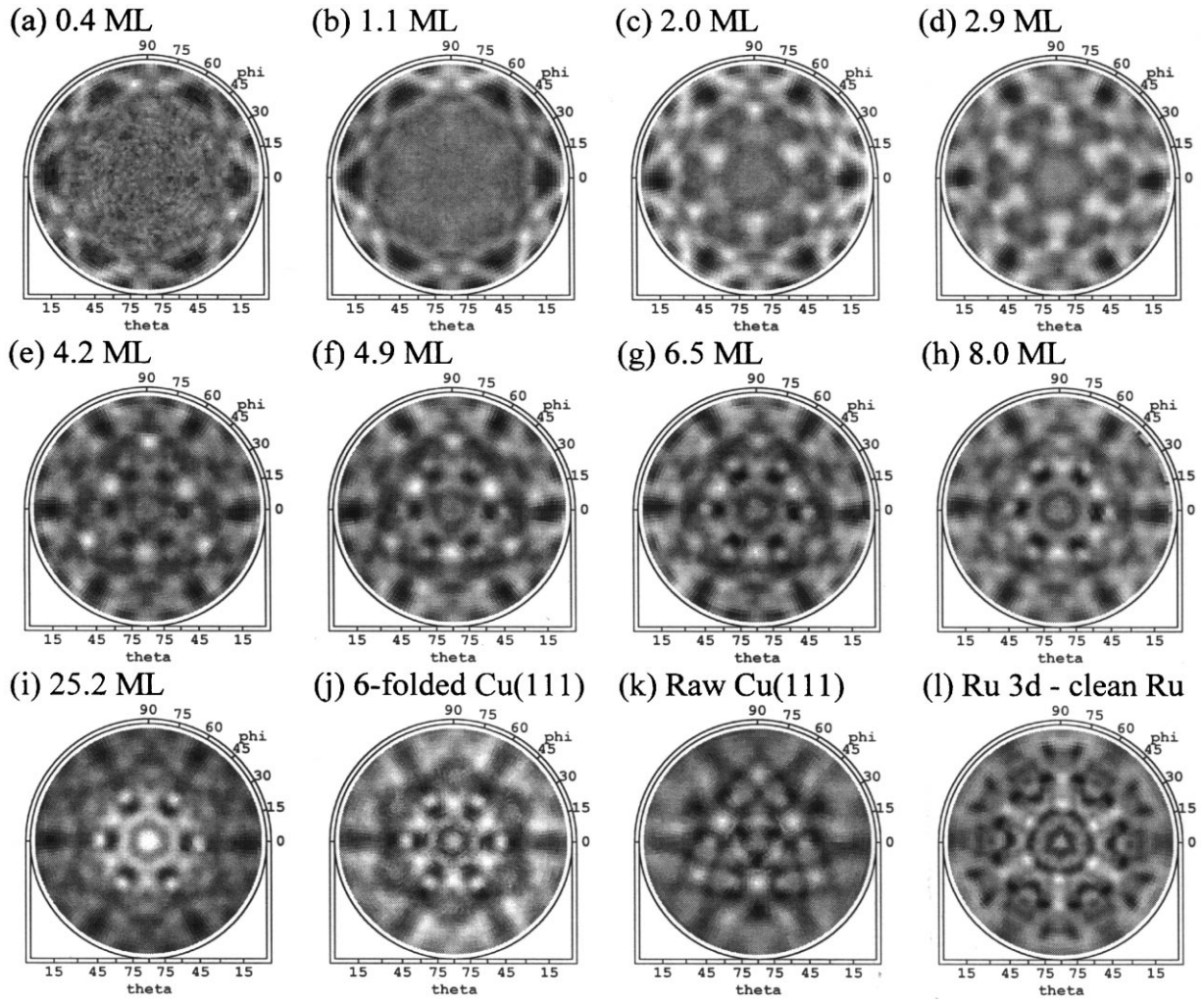

Fig. 2. (a)–(i) Experimental XPD patterns for Cu $2p_{3/2}$ emission ($E_{kin}=556$ eV) for several Cu coverages on clean Ru(0001): (a) 0.4 ML, (b) 1.1 ML, (c) 2.0 ML, (d) 2.9 ML, (e) 4.2 ML, (f) 4.9 ML, (g) 6.5 ML, (h) 8.0 ML, (i) 25.2 ML. (j) Experimental XPD patterns for Cu $2p_{3/2}$ emission from Cu(111) ($E_{kin}=556$ eV), as made artificially into a six-fold symmetry. (k) As (j), but raw data from Cu(111) with three-fold symmetry. (l) Experimental XPD pattern for Ru 3d emission ($E_{kin}=1206$ eV) from clean Ru(0001).

imental anisotropies suggests that the overlayer is Cu(111)-like, i.e. like fcc Cu(111), but with interlayer contractions and dislocations present. That is, peaks in the anisotropy first occur at 2 ML Cu coverage near 33–34° and also near 55°, in good agreement with the forward scattering directions for bulk Cu(111). The increase in the relative heights of these two anisotropy peaks with coverage is due to the increasing atomic chain lengths along these forward scattering directions. For a sufficiently thick layer (in fact 3 ML or more), a forward scattering peak near 70.5° should also appear, and in fact a small peak in the anisotropy near 70° does indeed appear at 25 ML. However, this feature is small enough that it may be strongly influenced by the higher-order interference effects from adjacent near-neighbor directions [24]. Shown in Fig. 3b and c are the corresponding anisotropies from MSC and SSC calculations, respectively, for 1–5 ML thick ideal clusters. (The

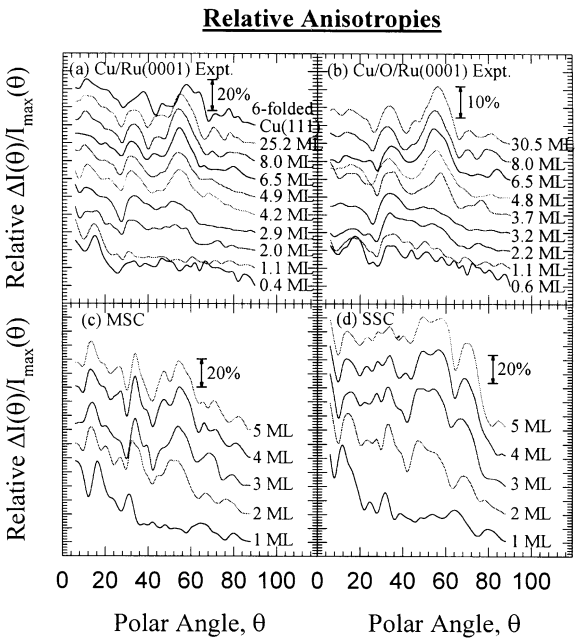

Fig. 3. (a) Experimental relative anisotropies $\Delta I(\theta)/I_{max}(\theta)$ versus polar angle for various Cu coverages from 0.4 to 25.2 ML on clean Ru(0001) and for bulk Cu(111) with six-fold symmetrization. Each value is calculated over a given azimuthal scan. These anisotropies range from 5 to 30%, depending on the polar angle. (b) As (a), but for various Cu coverages from 0.6 to 30.5 ML on Ru(0001) precovered with 0.5 ML O. The magnitudes of the anisotropies here are about half as large as those for Cu grown on clean Ru(0001). (c) As (a), but derived from multiple scattering cluster (MSC) calculations as described in the text. Here the magnitudes of the anisotropy are slightly larger than in the experiment. (d) As (b), but derived from single scattering cluster (SSC) calculations. Here, the magnitudes are often significantly larger than in the experiment.

way in which these calculations were performed is discussed in Section 3.1.2.) In general, the MSC curves agree very well with experiment as to peak positions and relative intensities, although the features in theory are often sharper than those in experiment. Beyond 2–3 ML, SSC theory diverges from MSC theory, and does not describe experiment as well. For example, due to the overly strong forward focusing in SSC calculations, the peak near 55° in the SSC anisotropy curves is too strong relative to MSC calculations and experiment. These differences between MSC and SSC will be discussed in more detail below when we fit theory to experiment for the entire XPD pattern.

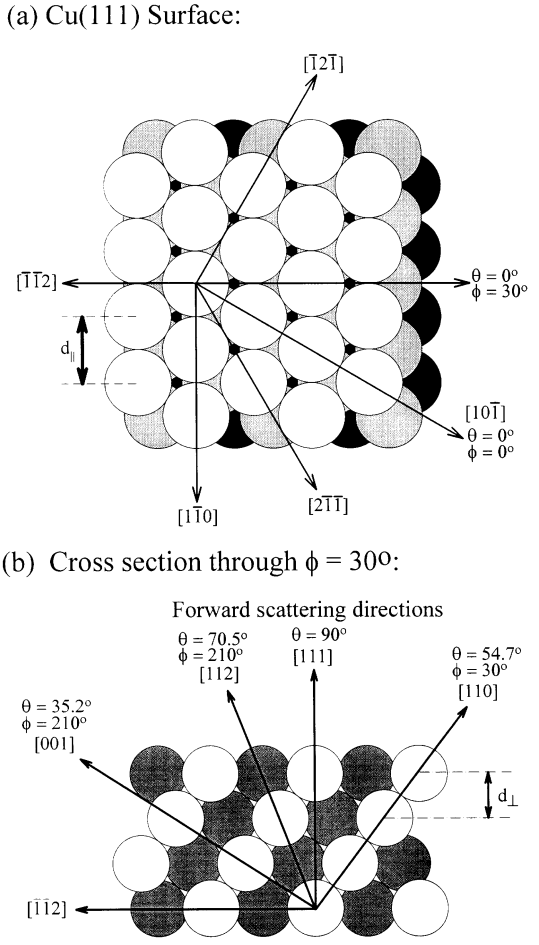

Fig. 4. (a) Atomic structure of the Cu(111) surface. The white circles represent the surface layer, the gray circles represent the second layer, and the black circles represent the third layer. Various low-index azimuthal directions are indicated. (b) A cross-section through a $(1\bar{1}0)$ plane at $\phi = 30°$, with various forward scattering directions indicated. The white circles represent atoms in the plane of the cut, and the gray circles represent atoms just behind the cut.

We now discuss qualitatively the full diffraction patterns in Fig. 2. In Fig. 2a and b, at 0.4 and 1.1 ML Cu coverages, respectively, we see no evidence whatsoever for forward scattering peaks. Thus, the XPD data provide a clear indication that the first layer is fully or nearly fully complete before the second layer begins to grow. In addition, the clear six-fold ring pattern at low θ is indicative of a pseudomorphic first layer of Cu on Ru. Two

sets of rings with six-fold symmetry rotated by 30° with respect to one another are seen. These are the first-order diffraction rings caused by photoelectrons emitted from one Cu atom and then scattered from the nearest- and next-nearest neighbor Cu atoms in a single hexagonal layer, and they have been seen before in adsorbate overlayer studies [26]. The polar angles at which these rings occur are in fact predicted quite well using a simple single-scattering calculation, i.e.

$$2\pi m = kr_k(1-\cos\theta_m)+\psi(\theta)_m, \quad m=1, 2, \ldots, \quad (3)$$

where θ_m is the polar angle, m is the diffraction order, r_k is the distance from an emitter to a given scatterer, $r_k(1-\cos\theta_m)$ is the path-length difference between direct and scattered waves, and $\psi(\theta_m)$ is the additional phase difference between direct and scattered waves produced by elastic scattering [24]. To account for surface refraction, θ_m inside the surface is then adjusted to θ'_m outside the surface according to

$$\theta'_m = \cos^{-1}[(1+V_0/E_{\mathrm{kin}})^{1/2}\cos\theta_m], \quad (4)$$

where V_0 is the surface inner potential and E_{kin} is the electron kinetic energy [24]. Using $V_0=14.4$ eV [35,36], the positions of the rings centered along $\phi=0°$, 60°, etc., due to nearest neighbors, are predicted to be at $\theta=28°$ along these directions and are observed at $\theta=26°$, and the positions of the rings centered along $\phi=30°$, 90°, etc., due to next-nearest neighbors, are predicted to be at $\theta=23°$ along these directions and are observed at $\theta=20°$. If we increase the inner potential to $V_0=21$ eV, this simple single scattering calculation gives ring positions which agree much better with the observed experimental positions. This may be a sign of an effectively higher inner potential for such low takeoff angles, but further, more careful experimental and theoretical work will be needed to confirm this suggestion. As further evidence for an effectively higher inner potential, the peak in anisotropy for 1 ML near 15° is about 1.5° higher in the MSC calculation than in experiment. According to Eq. (3), this peak position could be adjusted to match experiment by raising V_0 by about 8 eV to about 22 eV. But whether or not V_0 is adjusted, the first Cu layer has conformed to the substrate lattice geometry as a pseudomorphic layer, and to have the simple diffraction pattern associated with such a layer.

In Fig. 2c, at 2 ML Cu coverage, we still see the rings at low θ observed for ≤ 1 ML, but at a much higher $\theta\approx 50°$ three strong forward scattering peaks have appeared, indicating that the second layer has grown in the three-fold hollow sites of the first layer. In addition, these 2 ML results immediately suggest that the uniaxial striped dislocation structure seen in STM [2–5] threads itself all the way to the Cu–Ru interface, i.e. the first pseudomorphic layer uniaxially contracts with the second layer when the second layer is grown. If the underlying layers did not reconstruct with the top layer, then the underlying emitters would each see scatterers in the top layer in several different orientations, and this would tend to smear out the XPD pattern. The sharp diffraction pattern seen for 2 ML makes it clear that this is not the case, as we further confirm below with comparisons to theoretical calculations. For 2 ML, a second weaker set of three forward scattering peaks at $\theta\approx 50°$ is also seen, rotated 180° in ϕ from the first set. From this we conclude that the second-layer Cu atoms may sit in one of two possible three-fold sites of the first Cu layer, but with one of the two sites being preferred.

At 3 ML (Fig. 2d), a sharp six-fold pattern of strong forward scattering peaks at $\theta\approx 50°$ is seen, indicating that the Cu atoms still grow in the three-fold hollow sites of the underlying Cu layers, and further confirming that the dislocation structures seen in STM thread to the Cu–Ru interface. However, at 3 ML, no preference is shown for the two possible growth orientations on the Ru substrate, leading to full six-fold symmetry. At 3 ML, theoretical calculations to be discussed further below indicate that both fcc and hcp stacking will lead to a three-fold XPD pattern, although hcp appears slightly more six-fold and does not correctly converge to the correct six-fold pattern for thicker hcp layers (note the differences between the hcp Ru(0001) and sixfold Cu(111) patterns in Fig. 2j and l). Thus, if either type of stacking is to describe this data, the registry of the Cu layers with the Ru substrate must have two possible preferred orientations which are 180° apart in ϕ.

At 4 and 5 ML (Fig. 2e and f), a three-fold pattern with more fine structure at higher θ associated with a thicker fcc Cu(111)-like overlayer is observed. By 6.5 and 8 ML (Fig. 2g and h), a nearly six-fold pattern is observed which will be seen to be best described as a superposition of two fcc Cu(111)-like XPD patterns rotated by 180° in ϕ with respect to one another, and this six-fold pattern is also observed for a very thick Cu layer of 25 ML in Fig. 2i, as well as for the intentionally six-fold Cu(111) data in Fig. 2j. The six-fold pattern observed at these higher coverages cannot be attributed to equal amounts of fcc and hcp stacking of the Cu on itself, as an XPD pattern resulting from a thick hcp stacked layer is distinctly different from an XPD pattern resulting from a thick fcc stacked layer. For example, an hcp Ru 3d XPD pattern is shown in Fig. 2j, and it is very different to the patterns seen in the 6.5–25 ML range. Therefore, the cause of the six-fold symmetry at these higher coverages must be two fcc Cu(111) domains 180° apart in ϕ. A possible explanation for the two domains is the presence of monatomic steps on the Ru(0001) surface. With the ABABAB… stacking of the Ru hcp structure, we thus suppose that one orientation grows on an "A" terrace, whereas the other orientation grows on a "B" terrace. So, if we insert "/" between Ru and Cu, the two growth modes could be ABABA/BCABCABC… on an "A" step and ABABAB/CBACBACBA on a "B" step. However, this still does not fully explain the interesting changes in the symmetry of the XPD patterns between three-fold and six-fold as the coverage is increased, a point to which we will return below.

3.1.2. XPD: theoretical calculations

We now make a more quantitative comparison of our XPD results to theoretical calculations. These calculations were performed at both the single-scattering cluster (SSC) [28] and multiple-scattering cluster (MSC) [29,30] levels, using a separable Green's function method developed by Rehr and Albers [27]. This approximation has been used in second order (implying the use of 6×6 matrices), and recent extensive tests have shown this to be fully accurate for PD structural analyses [37]. Scattering phase shifts were calculated using a standard muffin-tin approximation and program [38]. The electron inelastic attenuation length in the Cu overlayer was estimated from the empirical equation $\Lambda_e(\text{Å}) = 0.54(E_{kin}[\text{eV}])^{0.5}$ [39,40]. Vibrational effects were included by Debye–Waller factors based on correlated vibrational motion, with the inputs being the bulk Cu Debye temperature and Debye wave vector [30,41]. An inner potential of 14.4 eV was used to allow for electron refraction in crossing the surface barrier (cf. Eq. (3)). As discussed earlier with reference to the diffraction rings at low θ for 1 ML, the effective inner potential at low takeoff angle may be higher than this value. We therefore varied the inner potential in MSC calculations for the case of 1 ML and performed an *R*-factor comparison (with *R*-factors defined below) between these calculations and experiment, and found that the *R*-factor minimum occurs at $V_0 = 21$ eV, in excellent agreement with the simple single scattering calculation performed earlier. An inner potential of 14.4 eV, however, was used in the calculations for all remaining coverages. The cluster sizes varied from 43 to 80 atoms, and are described for each of the cases below. In cases with >1 ML thickness, full advantage was taken of mirror-plane symmetry and the three-fold symmetry of Cu(111). That is, an emitter was placed in each Cu layer of the cluster, with the emitter being near the apex of a wedge of atoms spanning an angle somewhat greater than 60° to avoid edge truncation effects. The XPD calculations were then performed over the 60° azimuthal angular range of this wedge from $\phi = 30°$ to $\phi = 90°$. The intensities from these calculations were then mirrored across the $\phi = 90°$ plane and then three-fold mapped to 360°. The final intensity for such cases is then the sum over the intensities for all emitters. The angular broadening induced by the spectrometer was included by performing a standard multi-point average over a cone of 3.0° half angle [42]. However, we discuss below an additional angular broadening procedure which was found to improve the agreement with experiment. Before comparing to experiment, each theoretical pattern was converted to a normalized $\chi(\boldsymbol{k})$ by the same procedure used for the experimental patterns described above. Finally, because for-

ward scattering peaks along near-neighbor directions will be important features of such XPD patterns for layers ≥ 2 ML in thickness, we also show in the figures below for each cluster a figure in which each scatterer is represented by a circle or dot whose diameter is inversely proportional to the distance from the emitter. For clusters with emitters in more than one layer, the contribution from all emitters are superposed in these figures. Note that for the coverages with six-fold symmetry (such as 3 ML), we have six-fold symmetrized the corresponding forward scattering plots.

The *R*-factors used in this analysis are based on a set of five first discussed for LEED analyses [43] and then modified so as to be applicable to XPD by Saiki et al. [44]. The first quantity, R_1, is a normalized sum of the absolute value of the differences between the experimental and theoretical intensities. R_2 is a normalized sum of the square of the difference between the experimental and theoretical intensities, R_3 is the percentage of angle range over which the experimental and theoretical intensities have slopes of different sign ($\pm$), R_4 is a normalized sum of the absolute value of the difference between the first derivative of the experimental and theoretical intensities, and R_5 is a normalized sum of the square of the difference between the first derivatives of the experimental and theoretical intensities. These *R*-factors are discussed in more detail in Ref. [44]. These quantities have been determined by first calculating R_i at each individual polar angle in the nearly full 2π XPD pattern and then summing R_i over the polar angles from $\theta=6^\circ$ to $\theta=88^\circ$. We will refer to these summed *R*-factors as R_i^S. In most of our analysis, we have varied the interlayer spacing and calculated the resulting summed *R*-factors as a function of $d_\perp/d_\parallel$. In finally determining a structure, a global normalized-sum *R*-factor is then calculated by first normalizing $R_2^S-R_5^S$ to the average of R_1^S, i.e.

$$R_i^N(d_\perp/d_\parallel)=R_i^S(d_\perp/d_\parallel)\frac{\sum_{d_\perp/d_\parallel} R_i^S(d_\perp/d_\parallel)}{\sum_{d_\perp/d_\parallel} R_1^S(d_\perp/d_\parallel)},\quad i=2,3,4,5, \tag{5}$$

where $R_i^N(d_\perp/d_\parallel)$ is the *i*th normalized *R*-factor, and $R_1^N(d_\perp/d_\parallel)=R_1^S(d_\perp/d_\parallel)$. The global *R*-factor is then

$$R_{\text{global}}(d_\perp/d_\parallel)=\frac{1}{5}\sum_{i=1}^{5} R_i^N(d_\perp/d_\parallel). \tag{6}$$

These global *R*-factors have been determined by comparing experiment to SSC and MSC calculations on an fcc Cu lattice with various interlayer spacings and also various degrees of mixing between the two possible domains. The *R*-factor minima for both the interlayer spacing and relative domain occupation were determined in a self-consistent manner by iteratively finding the minimum *R*-factor for interlayer spacing and then finding the minimum *R*-factor for the relative domain occupation at this interlayer spacing. This process was then repeated until the minimum *R*-factors for interlayer spacing and for relative domain occupation were consistent with each other.

Another consideration emerging from this analysis is that theoretical XPD patterns, and in particular MSC XPD patterns, tend to show much more fine structure than experimental XPD patterns. This may be due to several reasons. One is that the $\pm 3^\circ$ angular broadening included in our calculations may not accurately represent the true amount of angular broadening in our experimental system, with the latter actually being slightly larger. In addition, there may be other effects in experiment such as defects and imperfections in the sample which tend to smear out the experimental XPD patterns as compared to theoretical XPD patterns. Finally, there may also be deficiencies in the way the MSC code includes the effects of both angular broadening and vibrational damping or smearing of diffraction structures. To account for such factors, we have thus also performed a systematic smoothing of the theoretical XPD patterns by convolution with a Gaussian of various widths, and this has in fact been found to lower the overall *R*-factors and improve the visual comparison with experiment. The Gaussian form represents a phenomologically reasonable shape to account for these additional factors. The Gaussian convolution procedure was developed by Len [45], and its application to XPD is described in more detail

elsewhere [13]. To illustrate the effects of this additional broadening, we show in Fig. 5a, the experimental XPD pattern at 5 ML, and in Fig. 5b–5e the MSC calculations at different degrees of Gaussian smoothing. Indicated next to each MSC calculation is the half width at half maximum (HWHM) of the gaussian used. Since a $\pm 3.0^\circ$ broadening has already been included in all of the MSC calculations in this work via a standard multi-point average, the amount of Gaussian smoothing indicated in Fig. 5b–5e represents additional smoothing. A simple (but always important) visual comparison of experiment and theory suggests that an HWHM somewhere in the range 2.4–4.8° provides the best fit to experiment, and in fact, the global *R*-factor is lowest at 4.8°. We also show in Fig. 6 a plot of the *R*-factor versus HWHM for both SSC and MSC calculations, and the minimum *R*-factor for both is at an HWHM of 4.0°–4.8°, although the curve for SSC is not as convincing due to other deficiencies in single scattering theory for describing a thick overlayer. The optimum broadening is thus slightly larger than the $\pm 3^\circ$ angular broadening used in our MSC code. The minimum MSC *R*-factor, in fact, is found to occur near an HWHM of 4.8° for all of our coverages. However, visual comparison suggests using an HWHM which is slightly smaller than this and thus, the theoretical XPD patterns shown in this paper have all been smoothed with a Gaussian of HWHM = 4.0°. We have, however, used the more quantitatively derived HWHM = 4.8° in all *R*-factor analyses for determining interlayer spacings and symmetries. Although the minimum *R*-factor at 1 ML also occured at an HWHM of 4.8°, we have used an HWHM of 2.4° at this coverage, again because the visual comparison seems much better. We have found that the choice of HWHM anywhere within the range of lowest *R*-factor to best visual comparison does not significantly affect the position of the *R*-factor minimum, although the overall *R*-factors are higher for smaller values of the HWHM.

The global *R*-factors used to determine interlayer spacings are shown in Fig. 7 for coverages from 1 ML up to 25 ML and for both SSC and MSC calculations. Due to the large amount of calculation time required for MSC calculations,

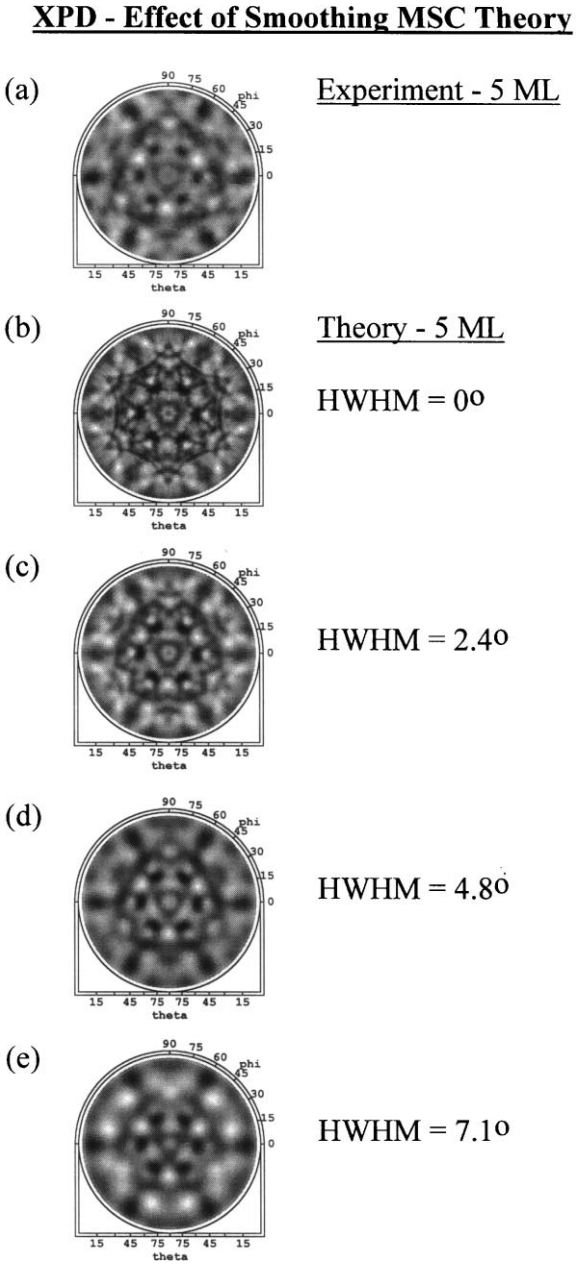

Fig. 5. Illustration of the effect of angular broadening by Gaussian smoothing on comparison of experiment and MSC theory. (a) 5.0 ML, experiment. (b) 5 ML, MSC theory without Gaussian smoothing (but with $\pm 3^\circ$ angular broadening using a multi-point average). (c) 5 ML, MSC theory smoothed with a Gaussian of half-width at half-maximum (HWHM) of 2.4. (d) As (c), but with HWHM = 4.8°. (e) As (c), but with HWHM = 7.1°.

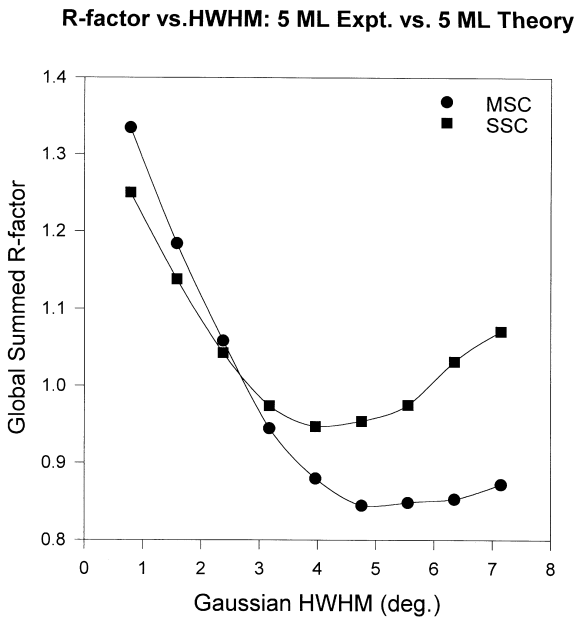

Fig. 6. Global sum over five normalized *R*-factors plotted for 5 ML SSC and 5 ML MSC calculations as compared to 5.0 ML experiment and for various degrees of Gaussian angular smoothing.

the cluster sizes have been limited to a maximum of 80 atoms. We have also performed single scattering calculations on larger clusters, and while the larger cluster size has the effect of changing the overall *R*-factor slightly, it does not significantly change the position of the *R*-factor minima, and therefore we only show single scattering *R*-factors for the smaller clusters. The curves through the *R*-factor points have been determined by spline interpolation. The positions of the *R*-factor minima and the corresponding uncertainties have been roughly estimated by adding 3% to the minimum in the *R*-factor curve, and using the half-width of the curve at this point as a measure of the $\pm$uncertainty. The minimum is then taken to be at the midpoint of this width. We note immediately in Fig. 7 that the SSC and MSC global *R*-factors agree very well up to 2.9 ML and then begin to diverge, with this divergence being much more severe for 4.9 ML and higher. For 2.0 ML and above, the MSC *R*-factor minima are always lower that those for SSC, and the shapes of the MSC curves are more well behaved in permitting the determination of a unique minimum. This is due to the onset of significant multiple scattering effects along chains of atoms for the thicker layers, and indicates that the MSC results should be much more reliable for such layers.

In Fig. 8a we present the experimental XPD pattern of the Cu $2p_{3/2}$ peak at 556 eV kinetic energy for a Cu coverage of 1 ML, and in Fig. 8b and c are the calculated XPD patterns using the MSC and SSC methods, respectively. The XPD calculations were performed on a cluster which consisted of a single Cu layer on top of an hcp Ru(0001) cluster, with the Cu atoms sitting in the three-fold hollow hcp sites of the Ru and at a vertical distance $Z_{\mathrm{Cu-Ru}}$ of 2.15 Å, corresponding the minimum of the *R*-factors in Fig. 7a. There were a total of 38 Cu atoms and 40 Ru atoms in the cluster. Although the SSC calculation for this simple bilayer case is in good agreement with experiment, and in fact yields a slightly lower minimum *R*-factor, the MSC calculation does better in a visual sense at predicting the fine structure, including particularly the two sets of first-order diffraction rings seen at low θ. These rings become much sharper and more like those seen in experiment in a multiple scattering simulation. This implies that multiple-scattering pathways via forward scattering along the surface are important in analyzing such XPD patterns, even though the single monolayer morphology of the Cu makes multiple scattering at higher angles from the surface negligible. The plot of the global *R*-factor versus the vertical distance $Z_{\mathrm{Cu-Ru}}$ in Fig. 5a has one other interesting feature: there are two minima of very nearly equal depth, one at 1.85 Å and one at 2.15 Å. This oscillation in the *R*-factor is due to pathlength-related variations of the phase between the direct photoelectron wave (emitted from the Cu monolayer) and its components scattered off the dominant nearest-neighbor Ru scatterers underneath. This type of behavior in XPD *R*-factors has been pointed out previously for the O/Ni system [43], and it is reminiscent of things also seen in LEED analyses [46,47]. This oscillatory behavior is not expected to happen at higher Cu coverages, as the *R*-factor now becomes primarily sensitive to changes in the direction of the dominant forward scattering peaks and their asso-

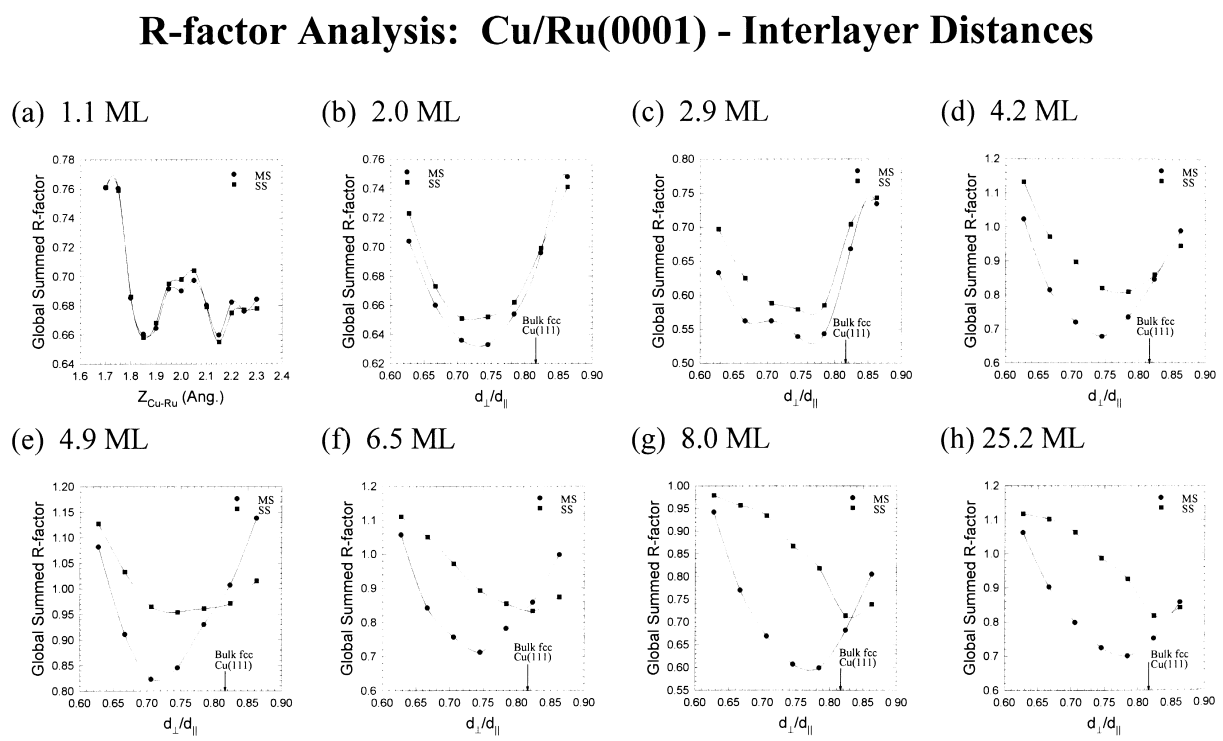

Fig. 7. Global *R*-factor plots versus the structural parameters $Z_{\mathrm{Cu-Ru}}$ or $d_{\perp}/d_{\parallel}$ and derived from comparing experiment to SSC and MSC calculations at various Cu coverages on Ru(0001). (a) 1 ML, (b) 2 ML, (c) 3 ML, (d) 4 ML, (e) 5 ML, (f) 6.5 ML, (g) 8 ML, (h) 25.2 ML. Note the divergence of results for SSC and MSC, which begins at about 4 ML as multiple scattering effects become more important. The fraction of occupation of domain #1 ($=f_1$) was also optimized for each case $\geq$2 ML, and is plotted in a later figure.

ciated higher-order fine structures, rather than changes in the backscattering from the substrate. The choice of the minimum at a vertical distance $Z_{\mathrm{Cu-Ru}}=2.15$ Å is in excellent agreement with prior LEIS [48] and LEED [49] experimental studies (which gave 2.10 ± 0.06 and 2.123 Å, respectively), as well as with LAPW theoretical calculations [49] (which gave 2.10 Å for Cu(1×1) growing in fcc sites on Ru(0001) and 2.07 Å for Cu(1×1)-hcp/Ru(0001)). This agreement is noteworthy, because at the high photoelectron kinetic energy ($E_{\mathrm{kin}}\geq500$ eV) studied here, XPD is not initially expected to be as sensitive a technique as LEED or LEIS for determining the substrate–overlayer distance, since photoelectron backscattering is weak at these higher energies. Nonetheless, we see that XPD can be used quantitatively for such cases, with the only caveat being the possibility of multiple minima in the *R*-factors.

For coverages of 2 ML and higher, the clusters for the MSC and SSC calculations consisted of the corresponding number of Cu layers with an fcc stacking sequence. Due to the weak backscattering at this high kinetic energy of 556 eV, Ru atoms were verified to have a negligible effect on these simulations for these thicker layers, and were thus omitted from the cluster. Although it is known from STM that a distribution of island heights exists on such surfaces [2–5], this distribution is generally peaked around the nominal thickness=coverage [5], and we have found it adequate to use this nominal thickness in our theoretical modeling. To best model the XPD patterns, which ranged from three-fold to six-fold symmetric depending on coverage, two three-fold fcc Cu(111) XPD patterns 180° apart in ϕ (denoted "1" and "2") were superimposed on each other and added with variable weighting factors f_1 and f_2, where

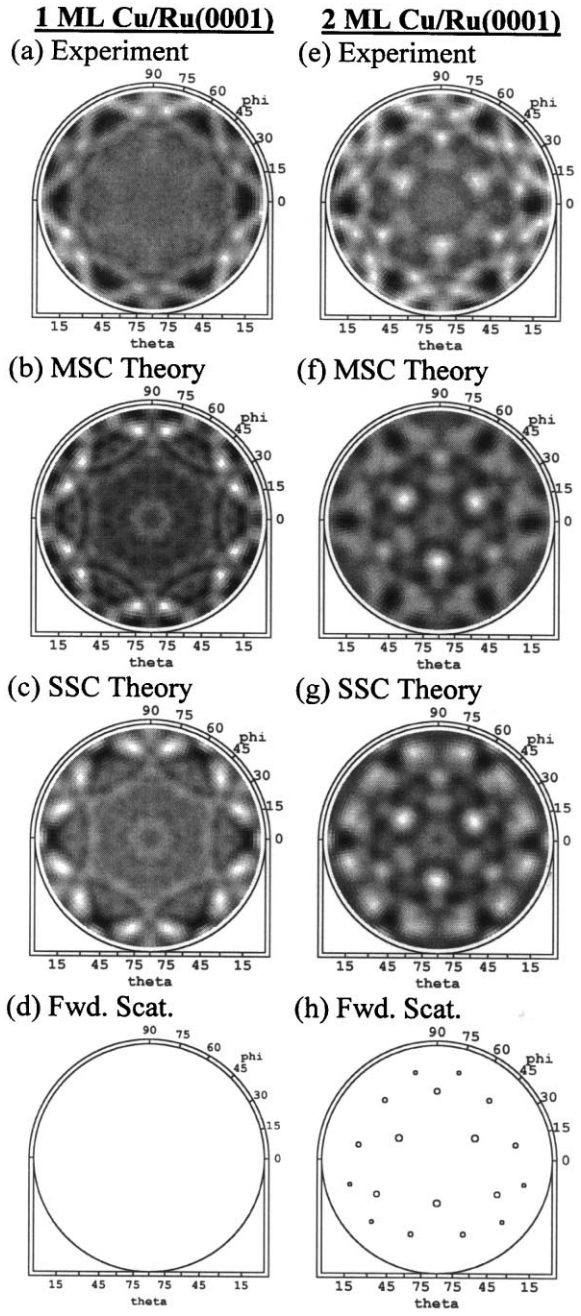

Fig. 8. Experimental and theoretical XPD patterns for Cu $2p_{3/2}$ emission. (a) 1.1 ML, experiment. (b) 1 ML, MSC theory. (c) 1 ML, SSC theory. (d) Positions of simple forward scattering directions in the 1 ML cluster, which in fact are not observable. (e) 2.0 ML, experiment. (f) 2 ML, MSC theory. (g) 2 ML, SSC theory. (h) Positions of simple forward scattering directions in the 2 ML cluster.

$f_2=(1-f_1)$. The in-plane Cu–Cu nearest-neighbor distance $d_\parallel$ in the calculations was set to 2.56 Å (as for bulk Cu(111)), and the Cu–Cu interlayer spacing $d_\perp$ was then varied to provide the best fit to experiment. We were thus able to finally determine the degree of interlayer relaxation via the ratio $d_\perp/d_\parallel$. The actual $d_\parallel$ may of course be slightly more than 2.56 Å due to interaction with Ru, and in fact it must vary from the 5.5%-expanded 2.70 Å for the pseudomorphic layer to 2.56 Å for the ultimate fully relaxed Cu(111). But the calculations are found to be primarily sensitive to $d_\perp/d_\parallel$, and only very weakly sensitive to $d_\parallel$ for a given $d_\perp/d_\parallel$. Also, we do not know how $d_\parallel$ will vary with coverage, so from this also it makes sense to analyze our data in terms of $d_\perp/d_\parallel$. Note also that the $d_\perp/d_\parallel$ values determined here represent an average over several Cu layers, with the top layers being weighted more heavily due to the greater amount of inelastic attenuation of photoelectrons emitted from deeper layers. The individual Cu–Cu interlayer spacings between different pairs of layers may vary slightly from this average, but we have not attempted to determine this.

Shown in Fig. 8e is the experimental 2 ML XPD pattern and in Fig. 8f and g the corresponding MSC and SSC XPD calculations, respectively. The 2 ML cluster consisted of 22 atoms in the first layer and 21 atoms in the second layer. The positions of the forward scattering peaks for this cluster are indicated in Fig. 8h, and they are in excellent agreement with the positions of the strongest diffraction peaks seen in experiment. The SSC calculation agrees reasonably well with experiment, but the MSC calculation is still better at predicting the fine structure, particularly at low θ, where multiple forward scattering is expected to be more important. A plot of the global R-factor versus $d_\perp/d_\parallel$ for 2 ML is shown in Fig. 7b, and it confirms the better description of MSC. The global R-factor minimum for SSC theory compared to experiment indicates that the Cu bilayer is significantly contracted from the bulk fcc Cu(111) interlayer spacing, with $d_\perp/d_\parallel=0.733\pm0.038$ in the bilayer and $d_\perp/d_\parallel=0.816$ for bulk Cu(111). The global R-factor minimum for MSC theory compared to experiment indicates that $d_\perp/d_\parallel=0.729\pm0.034$, in good agreement with SSC

theory. The *R*-factor analysis also indicates that, as averaged over different thicknesses, one of the two possible orientations of Cu on the Ru substrate is favored by a 3:2 ratio, thus yielding a value of $f_1 = 0.66$.

Shown in Fig. 9a is the experimental 3 ML XPD pattern, and in Fig. 9b and c the corresponding MSC and SSC XPD calculations, respectively. In addition, Fig. 9d shows a plot of the forward scattering directions for the cluster used in the MSC calculations. Initially, a 3 ML cluster consisting of 22 atoms in the first layer, 21 atoms in the second layer and 20 atoms in the third layer was used to compare to experiment. However, the 2 ML calculation not only appeared to be a better fit, but also gave lower overall *R*-factors, and we have thus used the 2 ML calculation (although with six-fold symmetry and thus $f_1 = f_2$) for comparison to the 3 ML experiment. We are able to justify this by the fact that, at the substrate temperature ($T \approx 600^\circ C$) at which we deposited Cu for 3 ML coverage, STM studies [5] indicate that the first two layers grow layer-by-layer while the third layer grows as very tall 3D islands which cover only about 10% of the surface. Thus, the XPD pattern is expected to be dominated by the first two layers, while the 3D islands are expected to contribute only a little to the XPD pattern. Both 2 ML calculations are in good agreement with experiment, but again the MSC calculation is in better agreement with the fine structure at low θ. A plot of the global *R*-factor versus $d_\perp/d_\parallel$ is shown in Fig. 5c. The *R*-factor minimum for experiment compared to SSC theory indicates that $d_\perp/d_\parallel = 0.740 \pm 0.026$, and that neither of the two possible orientations is favored: that is, they form in a 1:1 ratio with $f_1 = 0.50$, and so yield a six-fold pattern, as seen in experiment. The *R*-factor minimum for experiment compared to MSC theory indicates $d_\perp/d_\parallel = 0.756 \pm 0.018$, and the same 1:1 ratio is found. Although we can justify comparing 3 ML experiment to 2 ML theory, it is interesting to note that the 3 ML experiment is six-fold, whereas the 2 ML experiment is more three-fold. This is not a random effect, as the 2 ML and 3 ML experiments were repeated more than once and the symmetries did not change. It is not yet clear to us why this change in symmetry occurs,

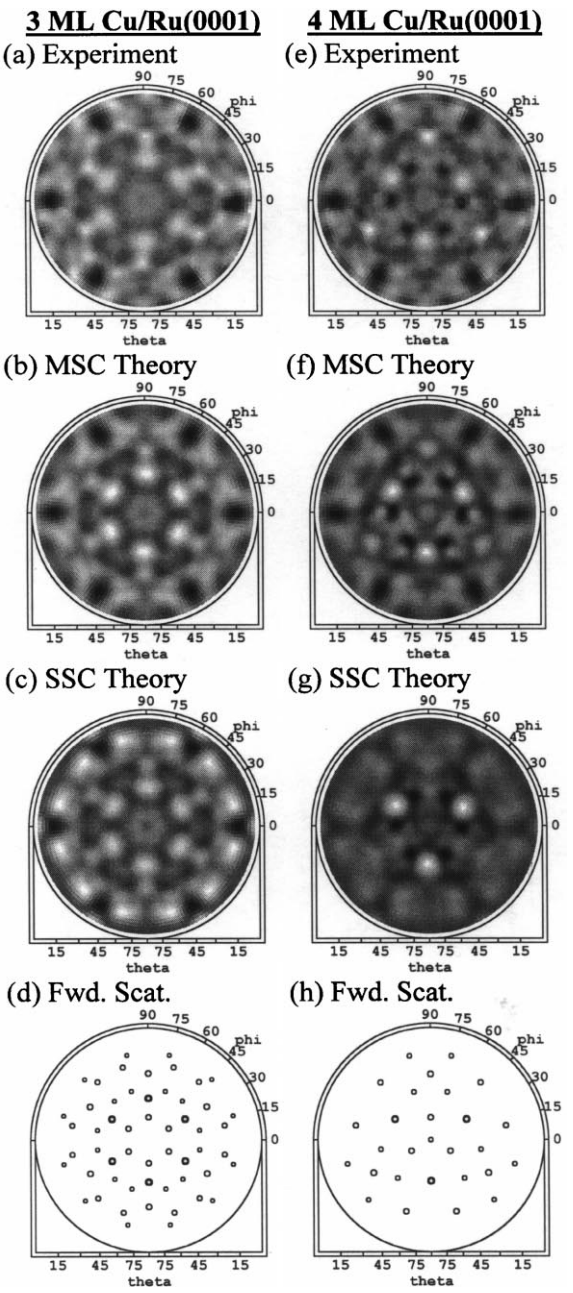

Fig. 9. Experimental and theoretical XPD patterns for Cu $2p_{3/2}$ emission. (a) 2.9 ML, experiment. (b) 2 ML, MSC theory (six-fold symmetrized). (c) 2 ML, SSC theory (six-fold symmetrized). (d) Positions of simple forward scattering directions in the 2 ML cluster (six-fold symmetrized). (e) 4.2 ML, experiment. (f) 4 ML, MSC theory. (g) 4 ML, SSC theory. (h) Positions of simple forward scattering directions in the three-fold symmetric 4 ML cluster.

but somehow having the extra monolayer of Cu for 3 ML forces the two domains of 2 ML growth into equal population.

Shown in Fig. 9e is the experimental 4.2 ML XPD pattern, while Fig. 9f and g show the 4 ML MSC and SSC XPD calculations, respectively, and Fig. 9h shows the forward scattering plot for the cluster used in the MSC calculation. The cluster consisted of 22 atoms in the first layer, 21 atoms in the second layer, 20 atoms in the third layer and 16 atoms in the fourth layer. As noted before, above 4 ML, our Cu films were grown at a substrate temperature of $T=300^{\circ}$C, where STM [5] predicts a more complete filling of each layer than for higher temperatures. Although the 4.2 ML film was heated briefly to 600°C, which should tend to promote the formation of 3D islands, we do not believe the 3D character is as great as in our 3 ML film since the anneal was very brief, and also due to the similarity of the 4.2 ML XPD pattern to the 4.9 ML XPD pattern. Thus, here we have used a 4 ML cluster to compare to experiment. For a 4 ML coverage in the fcc stacking, there are now multiple forward scattering paths along $\langle 110\rangle$-like directions (cf. Fig. 4b), and these directions are involved in the three strongest peaks seen in the SSC calculation. Here, the forward scattering peaks in the SSC calculation have become too strong due to a lack of consideration of multiple scattering [23–26]. That is, multiple scattering defocusing along chains of atoms reduces the intensities of forward scattering peaks [29,30], and thus the MSC calculation in Fig. 9f is in much better agreement with experiment over the full range of θ than the SSC calculation. An *R*-factor comparison of SSC calculations with experiment indicates that $d_{\perp}/d_{\parallel}=0.773\pm0.022$, and that one orientation is preferred again by about a 3:2 ratio ($f_1=0.66$). An *R*-factor comparison of MSC calculations to experiment indicates that $d_{\perp}/d_{\parallel}=0.742\pm0.016$, with the same domain ratio resulting. For this coverage, the $d_{\perp}/d_{\parallel}$ from SSC no longer agrees very well with $d_{\perp}/d_{\parallel}$ from MSC, as would be expected for a multilayer film where multiple scattering is expected to become more important. Above 4 ML, we thus do not expect the SSC analysis to be as accurate, although a preliminary set of calculations based on it is found to yield results in essential agreement with the main conclusions of this study [16].

Shown in Fig. 10a is the experimental 4.9 ML XPD pattern. Fig. 10b and c show the 5 ML MSC and SSC XPD calculations, respectively, and Fig. 10d shows the forward scattering plot. The cluster is the same as for the 4 ML MSC cluster, but with an added (bottom) fifth layer consisting of one atom. The XPD patterns have not changed significantly from the 4 ML XPD patterns, and this is true also for the anisotropy curve in Fig. 2. An *R*-factor comparison of SSC calculations with experiment indicates that $d_{\perp}/d_{\parallel}=0.769\pm0.047$, and that one orientation is preferred again by a 3:2 ratio ($f_1=0.66$). An *R*-factor comparison of MSC calculations with experiment indicates that $d_{\perp}/d_{\parallel}=0.718\pm0.018$. Both a visual comparison of the XPD patterns in Fig. 10a–c and the *R*-factor curves for this case in Fig. 7e makes it clear that the MSC result is the more reliable for $d_{\perp}/d_{\parallel}$.

Before proceeding to discuss the remaining experiment/theory comparisons in Figs. 10 and 11, we note that, due to multiple scattering defocusing as well as inelastic attenuation of the outgoing photoelectrons, only the top five or so atomic layers are expected to contribute significantly to the XPD patterns. Thus, MSC calculations for substrate emission are expected to converge in about 5–10 layers, as verified in this work and elsewhere [30,50]. To illustrate this effect for the present case, we show in Fig. 12 plots of MSC calculations for a Cu(111) cluster of 1–8 ML in thickness and with $d_{\perp}/d_{\parallel}=0.816$ as in bulk Cu. Visually, the MSC calculation appears to have converged by 5 ML, with no difference discernible among the 5, 6, 7 and 8 ML cases. To confirm this more quantitatively, we have performed an *R*-factor analysis in which the full pattern calculated for each coverage is compared to the 8 ML calculation, i.e. we have compared n ML to 8 ML for $n=1, 2, \ldots, 8$. A plot of this is shown in Fig. 13a. The *R*-factor decreases quickly between $n=1$ and $n=2$ and then continues to decrease by small amounts up to $n=8$, where it is required to go to zero from the 8 ML-to-8 ML comparison. If we now compare 8 ML experiment to each coverage in the MSC calculations from 1 to 8 ML, the *R*-factor also decreases quickly between 1 and 2 ML,

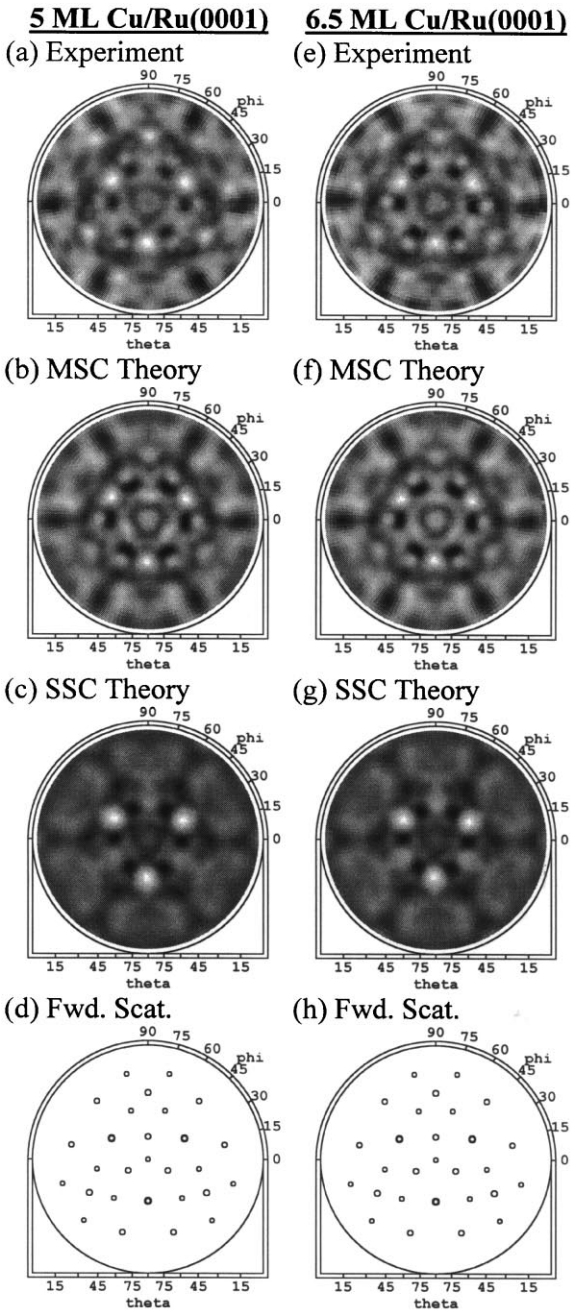

Fig. 10. Experimental and theoretical XPD patterns for Cu $2p_{3/2}$ emission. (a) 4.9 ML, experiment. (b) 5 ML, MSC theory. (c) 5 ML, SSC theory. (d) Positions of simple forward scattering directions in the 5 ML cluster. (e) 6.5 ML, experiment. (f) 5 ML, MSC theory. (g) 5 ML, SSC theory. (h) Positions of simple forward scattering directions in a 5 ML cluster.

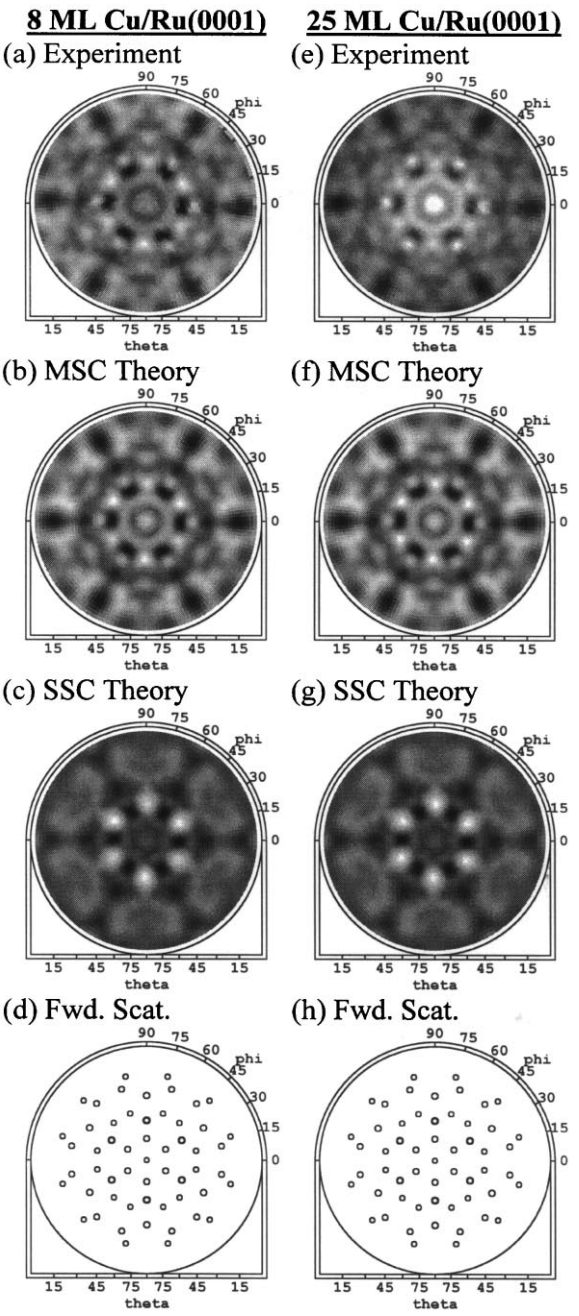

Fig. 11. Experimental and theoretical XPD patterns for Cu $2p_{3/2}$ emission. (a) 8.0 ML, experiment. (b) 5 ML, MSC theory. (c) 5 ML, SSC theory. (d) Positions of simple forward scattering directions for a 5 ML cluster (six-fold symmetrized in order to simulate two domains). (e) 25.2 ML, experiment. (f) 5 ML, MSC theory. (g) 8 ML, SSC theory. (h) Positions of forward scattering directions for a 5 ML cluster.

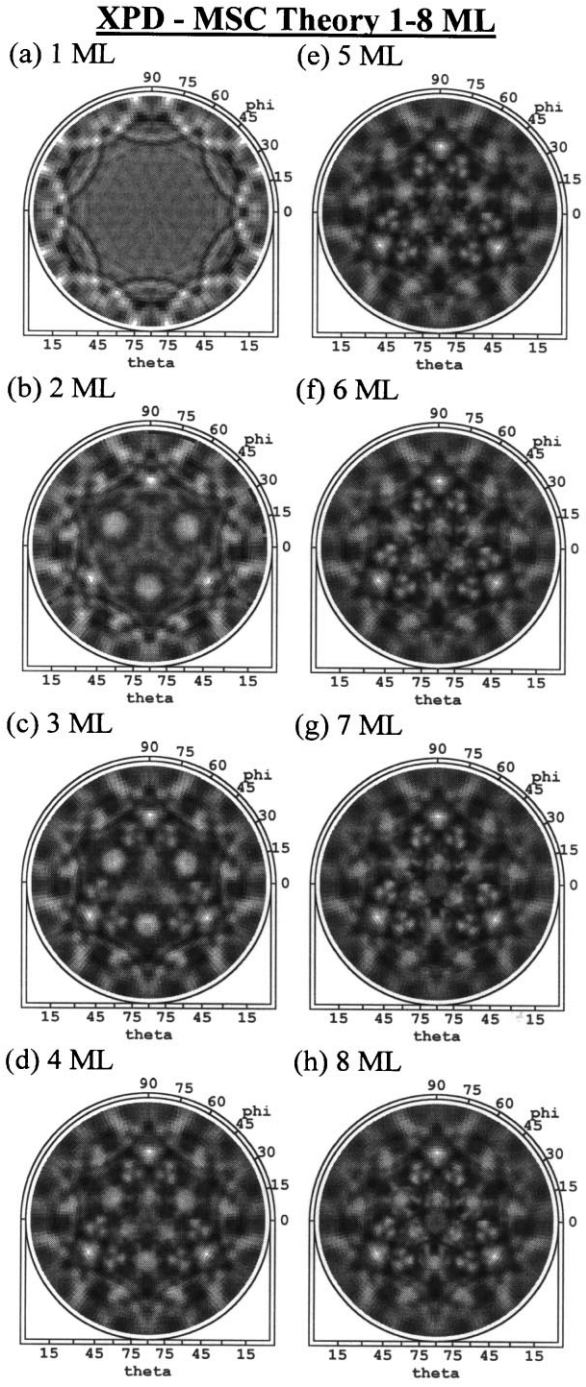

Fig. 12. MSC calculations from (a) 1 ML up to (h) 8 ML for the bulk value of $d_{\perp}/d_{\parallel}=0.816$. Visually, the MSC calculation appears to have converged to a bulk-like description by about 5 ML.

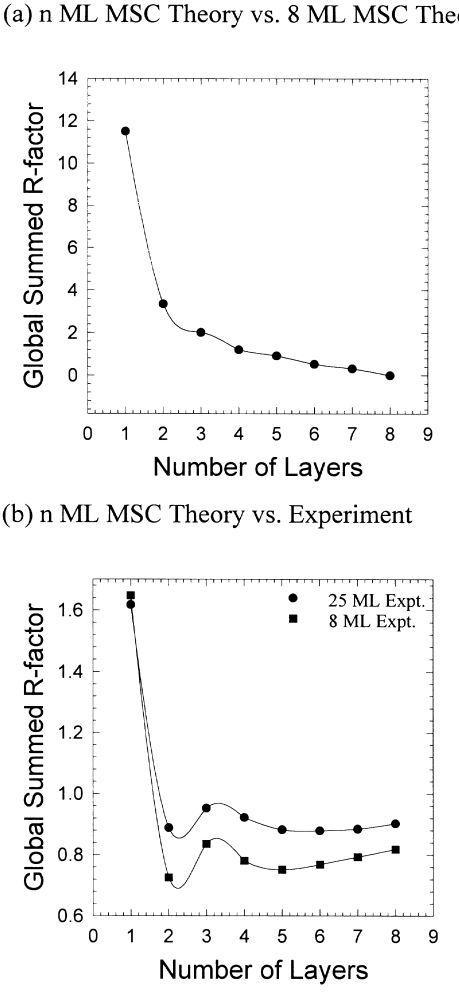

Fig. 13. (a) Global *R*-factor comparison of MSC theory for *n* ML to MSC theory for 8 ML, as shown in Fig. 12. (b) Global *R*-factor comparison of 25.2 ML experiment and 8 ML experiment to *n* ML theory for $n=1, 2, \ldots, 8$.

increases a little between 2 and 3 ML, decreases a little between 3 and 5 ML, and then increases by very small amounts up to 8 ML. A plot of this is shown in Fig. 13b. Due to the large amount of computation time needed to perform MSC calculations on several layers, we have only been able to go up to 8 ML. Although these comparisons of theory with theory and of experiment with theory do not indicate a complete convergence by 8 ML, using thicker layers for interlayer determination would not significantly change our results. We

conclude from Figs. 12 and 13 that a 5 ML cluster should yield a very good agreement with experiment. In particular, since the shapes and sizes of the peaks and diffraction features in the XPD patterns as well as the positions of the peaks and features do not change significantly after about 5 ML, the small change in the *R*-factor for each successive layer thickness must be due to small subtle changes in the relative intensities of the peaks and features in the XPD pattern. Thus, it should not be necessary to perform MSC calculations on clusters much thicker than about 5 ML in order to model thicker experimental overlayers, and this should be a generally useful rule for analyzing epilayers of low-to-medium Z materials with XPD.

Due to the foregoing discussion and the large amount of computation time required to perform MSC and SSC calculations on multilayer clusters with several emitters, we have thus only performed extensive calculations for geometry determinations with clusters from one to five Cu layers. Therefore, Fig. 10e shows the experimental 6.5 ML XPD pattern, while Fig. 10f and g represent XPD calculations for a 5 ML cluster in MSC and SSC, respectively. The forward scattering plot is also shown in Fig. 10h. By 6.5 ML, the symmetry of the experimental 6.5 ML XPD pattern is beginning to appear more six-fold, and in fact an *R*-factor comparison of SSC calculations with experiment indicates that one orientation is now preferred by only a 5:3 ratio ($f_1=0.60$) and that $d_\perp/d_\parallel=0.812\pm0.026$. An *R*-factor comparison of MSC calculations with experiment further indicates that $d_\perp/d_\parallel=0.740\pm0.014$, and we expect this to be the most reliable of the two determinations.

Shown in Fig. 11a is the experimental 8 ML XPD pattern, which is now essentially sixfold, and in Fig. 11b and c are the 5 ML MSC and SSC calculations, respectively. Here, the SSC calculation again does not model experiment very well due to the too-great strength of the dominant forward scattering peaks at $\theta\approx52^\circ$. However, the MSC calculation with an equal mixture of the two orientations ($f_1=0.50$) matches experiment very well. An *R*-factor comparison of SSC calculations to experiment indicates that $d_\perp/d_\parallel=0.837\pm0.016$. Comparison of the more accurate MSC calculations to experiment indicates that $d_\perp/d_\parallel=0.766\pm0.018$.

Shown in Fig. 11e is the experimental 25 ML XPD pattern, and in Fig. 11f and g are the 5 ML MSC and SSC calculations, respectively. An *R*-factor comparison of SSC calculations to experiment indicates that $d_\perp/d_\parallel=0.835\pm0.014$ and that neither orientation is preferred ($f_1=0.50$). In contrast, our most accurate MSC analysis of the XPD data indicates that $d_\perp/d_\parallel=0.777\pm0.020$, again with $f_1=0.50$. Thus, the MSC analysis for 25 ML indicates that the near-surface average Cu interlayer spacing is still contracted by about $4.8\pm2.5\%$ from bulk fcc Cu(111). This is not a completely surprising result, as such contractions from bulk values have been observed in other metal-on-metal systems, such as Ni/Cu(001) [51,52]. A LEED *I–V* structure determination of the Ni/Cu system also indicates that the average interlayer distance in the top five or so layers of an 11 ML Ni film is 1.72 ± 0.03 Å, or about 2.3% smaller than the bulk interlayer distance of 1.76 Å [51,52].

We now summarize the predictions of the MSC analysis for $d_\perp/d_\parallel$ in Fig. 14a, and for the determination of the pattern symmetry and f_1 in Fig. 14b. Also shown in Fig. 14a is a theoretical estimate of $d_\perp/d_\parallel$ versus coverage in which we have taken areal Cu densities derived from 2D Frenkel–Kontorova calculations by Hamilton and Foiles [6], used these to derive $d_\parallel$, and then assumed a constant atomic volume to estimate $d_\perp$. This theoretical estimate suggests a fairly rapid convergence to the bulk $d_\perp/d_\parallel=0.816$ by 4 ML. For coverages of 2 and 3 ML, comparison of our XPD results with MSC calculations yields $d_\perp/d_\parallel$ values which agree rather well with this simple theoretical estimate. In contrast, for coverages from 4 to 8 ML, comparison of our data to to MSC calculations indicates a much slower convergence to the bulk Cu(111) interlayer spacing and suggests that the top five or so layers of the Cu overlayer have not quite converged to bulk Cu(111) interlayer spacings even up to 25 ML coverage. As another method of estimation, we have also used elasticity theory considering trigo-

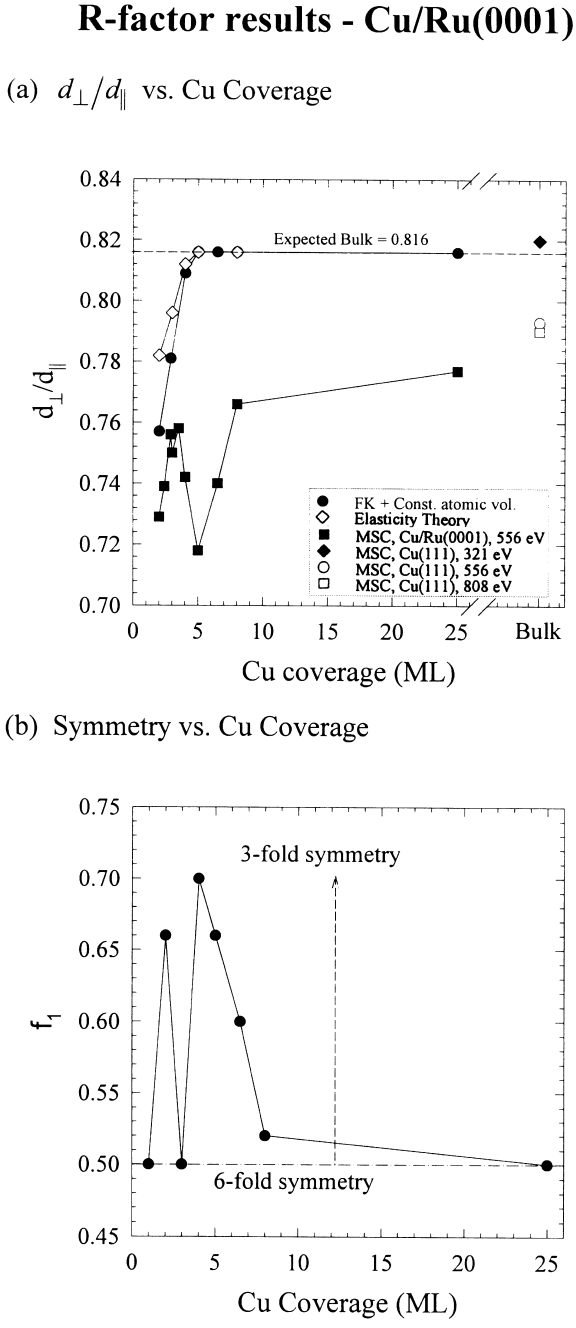

Fig. 14. (a) Plot of $d_\perp/d_\parallel$=(Cu–Cu interplanar distance)/(Cu–Cu in-plane nearest-neighbor distance) versus coverage in monolayers (ML), as derived by different methods. ●, estimate of $d_\perp/d_\parallel$ using Cu areal densities derived from a 2D Frenkel–Kontorova model by Hamilton and Foiles [6] combined with a constant atomic-volume assumption. ◇, estimate of $d_\perp/d_\parallel$ using Cu areal densities derived from a 2D Frenkel–Kontorova model by Hamilton and Foiles [6] combined with elasticity theory [57,58]. ■, $d_\perp/d_\parallel$ determined by *R*-factor comparisons between experimental XPD data from various Cu coverages on Ru(0001) and MSC calculations for Cu $2p_{3/2}$ emission at a photoelectron kinetic energy of 556 eV. ◆ and □, $d_\perp/d_\parallel$ determined by *R*-factor comparisons to experimental Cu $2p_{3/2}$ data obtained from Cu(111) by Naumović and Osterwalder at photoelectron kinetic energies of 321 and 808 eV, respectively [31]. ○, $d_\perp/d_\parallel$ determined by an *R*-factor comparison between experimental Cu $2p_{3/2}$ XPD data obtained in our laboratory from a Cu(111) single crystal and MSC calculations at an energy of 556 eV (b) Plot of the relative occupation of domain #1 versus coverage, with rotational symmetry indicated.

nal strain [53–57]. That is, $d_\parallel$ was again taken from the Frenkel–Kontorova analysis, and elasticity theory was then used to predict $d_\perp$ [13]. Elasticity theory predicts an even more rapid approach to the bulk values, as shown in Fig. 14a. Taken together, these experimental results thus indicate a much higher degree of interlayer relaxation for thinner layers than predicted by applying either a constant volume assumption or elasticity theory to the results of the simple Frenkel–Kontorova model. This contraction has additional potential implications for the chemical reactivity of such Cu layers.

In Fig. 14b we present a plot of the fractional occupation of domain #1 (f_1) as a function of coverage. At 1 ML, the six-fold symmetry is expected, as an emitting atom in the pseudomorphic overlayer will have six nearest neighbors in a hexagonal pattern around it, thus producing the ring pattern in Fig. 2a and b. At the higher coverages, for fcc growth in a single domain, the XPD pattern will be three-fold (cf. Fig. 2k), but for fcc growth in two equally populated domains 180° apart in ϕ, the XPD pattern will be six-fold (cf. Fig. 2j). We noted interesting changes in the symmetry as we increased the coverage from 2 to 8 ML. At 2 ML, the symmetry is three-fold, indicating a preference for a particular adsorption site of the second-layer atoms on the first Cu layer. According to STM [2–5] results, the uniaxial contraction may take place in three directions, 120° apart in ϕ. However, this will not produce the

three-fold symmetry seen in XPD since the technique is not sensitive to the long-range features of the overlayer, but is rather a short-range structural probe of the near-neighbor Cu atoms in the overlayer which can contribute to forward scattering and other diffraction features. Thus, locally, the structure is fcc Cu(111)-like, and the three-fold pattern results. At 3 ML, however, the symmetry is six-fold, and thus at 3 ML, the two possible domains of fcc Cu(111) on Ru(0001) have become equally populated. We have commented before on the fact that this layer tends to be dominated by a 2 ML surface, with small, thick islands to accommodate the additional material. At 4 and 5 ML, the symmetry becomes three-fold again, and finally the pattern returns to nearly six-fold symmetry at 8 ML and above, converging to the case of equal occupation of the two domains by 25 ML. A possible explanation for the jump to six-fold symmetry at 3 ML may be that, according to STM data [5], the substrate temperature during the deposition of three or more monolayers will significantly change the amount of 3D islanding. That is, at lower temperatures the growth is more layer-by-layer with the 3D islands covering a large area of the surface, while at higher temperatures, the 3D islands grow thicker and covers less of the surface. Between 3 and 5 ML, we lowered our substrate temperature, and thus our 5 ML film should be smoother than our 3 ML film. At thicker coverages above about 8 ML, more 3D islanding occurs, regardless of the deposition temperature. Perhaps the 3D islands allow for more randomness in domain occupation, whereas when the growth is more layer-by-layer, the film coalesces into a single domain. However, this would tend to suggest that our 4.2 ML film, which was annealed at 600°C, should be more six-fold due to the occurrence of 3D islanding. But we only annealed this sample for a short time, and it may not have been able to attain as much 3D character as the 3 ML film which was at 600°C during deposition and also for a brief time after deposition before cooling. Thus, at coverages where more 3D islanding occurs, we expect the symmetry to be more six-fold, and at coverages where the film is smoother, the symmetry should be more three-fold.

3.1.3. Reference XPD results for bulk Cu(111) and comparison to theory

In assessing the accuracy of our XPD analysis, it is important to verify that it converges to a correct interlayer spacing for the limiting case of bulk Cu(111). Thus, we have compared MSC calculations at three photoelectron kinetic energies of 321, 556 and 808 eV to Cu $2p_{3/2}$ experimental XPD patterns taken from a Cu(111) single crystal at these energies. The data at 321 and 808 eV were obtained by Naumović and Osterwalder [32,33], and made use of somewhat better angular resolution than ours. The data at 556 eV were obtained with the same system as all of the other patterns shown here, and have already been presented in Fig. 2k. Shown first in Fig. 15a is the experimental 321 eV XPD pattern, and in Fig. 15b and c are the corresponding MSC and SSC calculations, respectively, for the optimized interlayer spacing. Shown in Fig. 15d is the experimental 556 eV XPD pattern, and in Fig. 15e and f are the corresponding MSC and SSC calculations, respectively. Shown in Fig. 15g is the experimental 808 eV XPD pattern, and in Fig. 15h and i are the corresponding MSC and SSC calculations, respectively. The MSC patterns are in excellent agreement with experiment, while the SSC patterns have overly strong forward scattering peaks, as noted previously. An *R*-factor comparison of the 321 eV XPD pattern to MSC indicates that $d_\perp/d_\parallel = 0.820 \pm 0.020$, about 0.5% larger than the bulk. An *R*-factor comparison of the experimental 556 eV XPD pattern to MSC indicates that $d_\perp/d_\parallel = 0.792 \pm 0.023$, about 2.9% smaller than the bulk. An *R*-factor comparison of the experimental 808 eV XPD pattern to MSC indicates that $d_\perp/d_\parallel = 0.792 \pm 0.017$, about 2.9% smaller than the bulk, and in excellent agreement with the 556 eV result. Plots of the MSC global summed *R*-factor for 321, 556 and 808 eV XPD patterns are shown in Fig. 16, and Fig. 14a also shows the three Cu(111) interplanar distances determined from XPD as open symbols, with two points overlying one another. The average $d_\perp/d_\parallel$ over these three sets of Cu(111) data is thus 0.801, corresponding to a small interlayer contraction of -1.8% (-0.04 Å). Our overall error estimate for these numbers based on the 3% criterion on change in

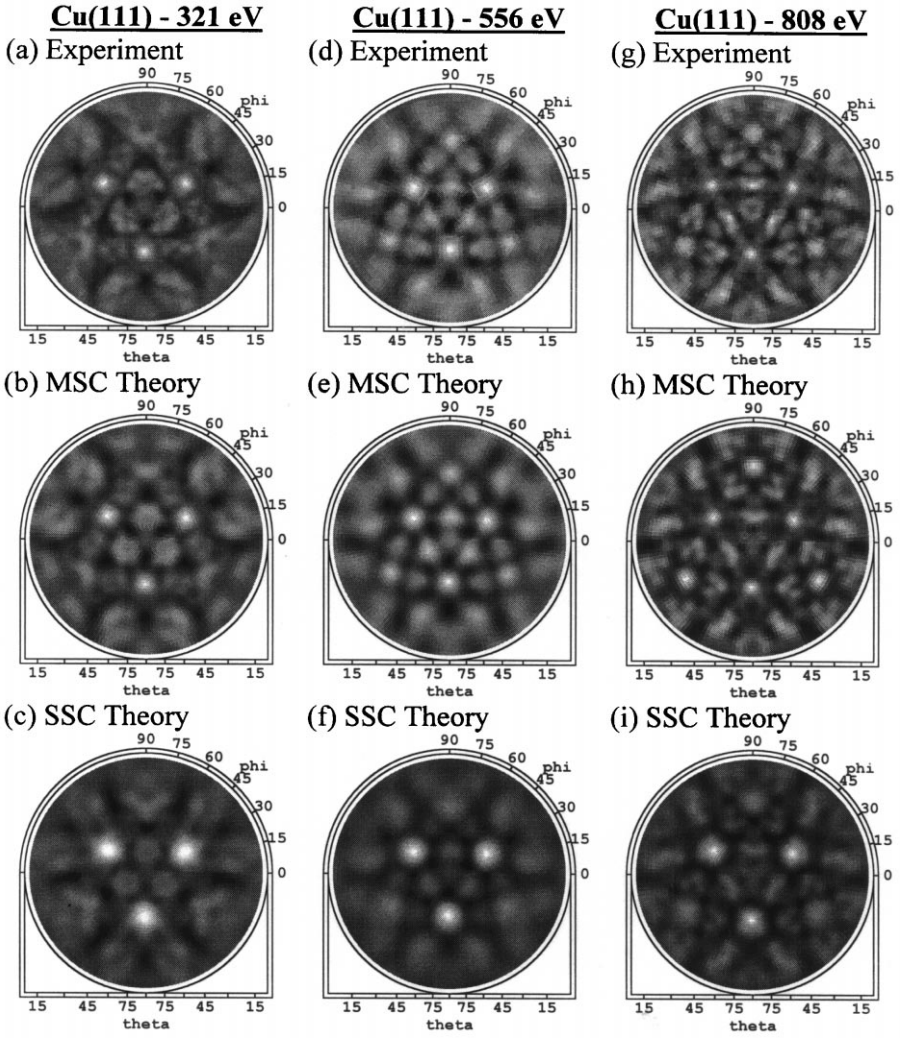

Fig. 15. Experimental XPD patterns for Cu $2p_{3/2}$ emission at three different energies from from a Cu(111) single crystal, as compared to corresponding MSC and SSC calculations for the optimum interlayer spacing. (a)–(c) Kinetic energy of 321 eV. (d)–(f) Energy of 556 eV. (g)–(i) Energy of 808 eV. The 321 and 808 eV data are from Naumović and Osterwalder [31].

R-factor is $\sim \pm 4.2\%$ (± 0.09 Å), and thus includes the case of no relaxation. For comparison, prior LEED studies of Cu(111) yield varying results for the topmost interlayer distance. Watson et al. [53] reported a surface relaxation of $-4.1 \pm 0.6\%$ (-0.085 ± 0.012 Å) for Cu(111), in good agreement with our results. Tear et al. [54] reported a very small surface relaxation of $-0.3 \pm 1\%$ (-0.006 ± 0.021 Å). Neve et al. [55] found the topmost copper layer to be relaxed by a somewhat larger space, i.e. -0.6% (-0.012 Å). Finally, Bartos et al. [56] found a $+0.8 \pm 1.0\%$ ($+0.016 \pm 0.021$ Å) expansion of the topmost Cu layer. These LEED values thus span essentially the same range as our XPD analysis, and a simple arithmetic average of them yields a -1.06% (-0.022 Å) contraction, although we stress that LEED measures the relaxation of the topmost layer, whereas we are measuring an average over the first five layers, but with strong weighting toward the first few. Thus, within our range of error, our XPD results for $d_{\perp}/d_{\parallel}$ for a thick Cu

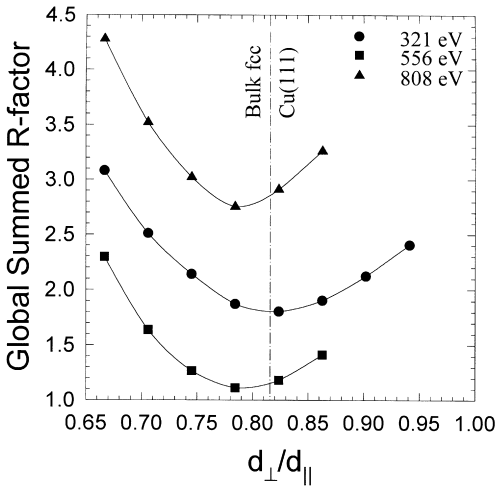

Fig. 16. Global summed *R*-factor plot for MSC comparisons to the Cu(111) data shown in Fig. 15a, d and g.

film of 25 ML grown on Ru(0001) are lower than, but still can be considered to agree reasonably well with, similar results obtained from a Cu(111) single crystal and from prior LEED analyses of the Cu(111) surface.

3.2. Cu grown on O-precovered Ru(0001)

3.2.1. Experimental results and comparison to Cu on clean Ru(0001)

Finally, we consider the effect on the Cu growth modes of preadsorbing oxygen on Ru(0001). First we show for reference in Fig. 17a the XPD pattern of the experimental O 1s ($E_{kin}=958$ eV) peak for O/Ru(0001) at an oxygen saturation coverage of 0.5 ML, and in Fig. 17b and c the corresponding MSC and SSC calculations, respectively, as summed over the three domains of p(2×1)-O/Ru(0001) expected on this surface. For reference to the substrate, the experimental Ru 3d XPD pattern is shown in Fig. 17d. Due to the weak photoelectric cross-section of the O 1s peak, the experimental data were rather noisy, and therefore the diffraction features at low θ were very faint in the initial XPD pattern. Thus, a more quantitative analysis of this data is not possible. For presentation purposes, we have also applied a significant amount of smoothing as well as symmetrization through a mirror plane on the experimental XPD

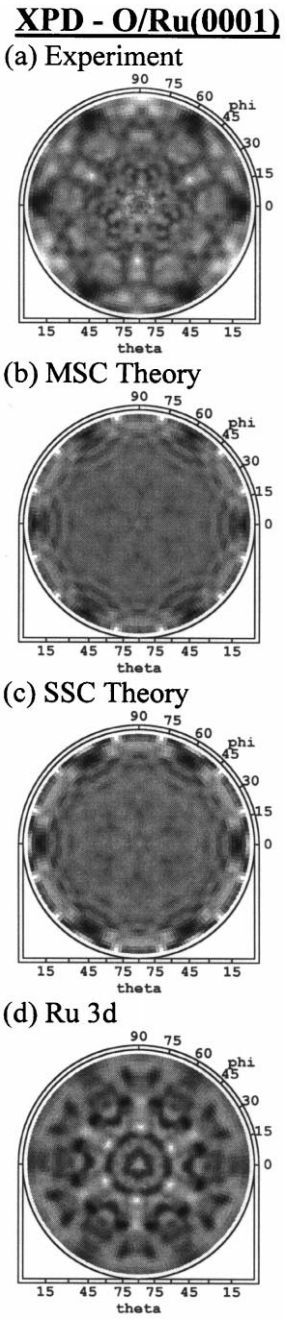

Fig. 17. XPD patterns from a 0.5 ML saturation coverage of oxygen on Ru(0001) for (a) experimental O 1s peak, (b) MSC calculation of O 1s peak, assuming three domains of p(2×1)-O/Ru(0001), (c) as (b), but SSC calculation, (d) experimental Ru 3d peak with a covering of 0.5 ML O (cf. Fig. 2l).

pattern shown in Fig. 17a. The final anisotropy is very small, being only about 15% over an azimuthal scan at $\theta = 12^\circ$, for which it is a maximum. Also, the features seen at high θ in the experimental XPD pattern are largely artifacts of the smoothing and symmetrization process. The Ru 3d XPD pattern is essentially identical to that for the clean surface, although the features at lower θ maybe somewhat weaker due to scattering in the O overlayer. Oxygen forms an ordered $p(2\times1)$ structure on Ru at the saturation coverage of 0.5 ML [59], although according to LEED it appears to form a $p(2\times2)$ structure due to the occurrence of three possible domains of $p(2\times1)$-O. The actual $p(2\times2)$ structure will form at an oxygen coverage of 0.25 ML, but is not possible at an oxygen coverage of 0.5 ML. The experimental O 1s XPD pattern shown in Fig. 17a has a six-fold symmetry for low polar angles and weak three-fold symmetry at higher angles. At low polar angles, there is also an indication of first-order diffraction rings similar to those in Fig. 2a and b which would have to be due to near-neighbor forward scattering in three $p(2\times1)$-O domains 120° apart in azimuth. The MSC and SSC calculations have the correct six-fold symmetry and are in good qualitative agreement with experiment, also showing strong minima at low θ and at $\phi = 0^\circ$, 60°, 120°, etc.

For the Cu overlayers, we begin by considering the plots of the relative azimuthal anisotropies of the Cu $2p_{3/2}$ XPD patterns for Cu/O/Ru(0001) as a function of the polar angle, as shown in Fig. 3b. For 2 ML and above, the anisotropies have very nearly the same shape as the anisotropies shown for Cu/Ru(0001) in Fig. 3a. This similarity in anisotropy curves is an indication that the structure of the Cu overlayer is not significantly changed by the addition of oxygen for thicker overlayers, even though the deposition parameters for the two sets of overlayers are also very different. However, at 1 ML, the shape of the anisotropy curve is different for Cu/O/Ru(0001) and Cu/Ru(0001), and in fact that for Cu/O/Ru(0001) looks more like that for 2 ML of Cu/Ru(0001). This suggests that double-layer stacking occurs at 1 ML in Cu/O/Ru(0001). The absolute anisotropies for Cu/O/Ru(0001) and for Cu/Ru(0001) also differ, with those for Cu/O/Ru(0001) being only about half as high as the anisotropies for Cu/Ru(0001).

In Figs. 18–21 we show O 1s and Cu $2p_{3/2}$ XPD results for Cu grown on oxygen-precovered Ru(0001), and compare them directly to the corresponding Cu $2p_{3/2}$ results for Cu grown on clean Ru(0001) (shown in the bottom panels of each column). In Fig. 18a and d we show XPD results for the O 1s peak, and in Fig. 18b and e the

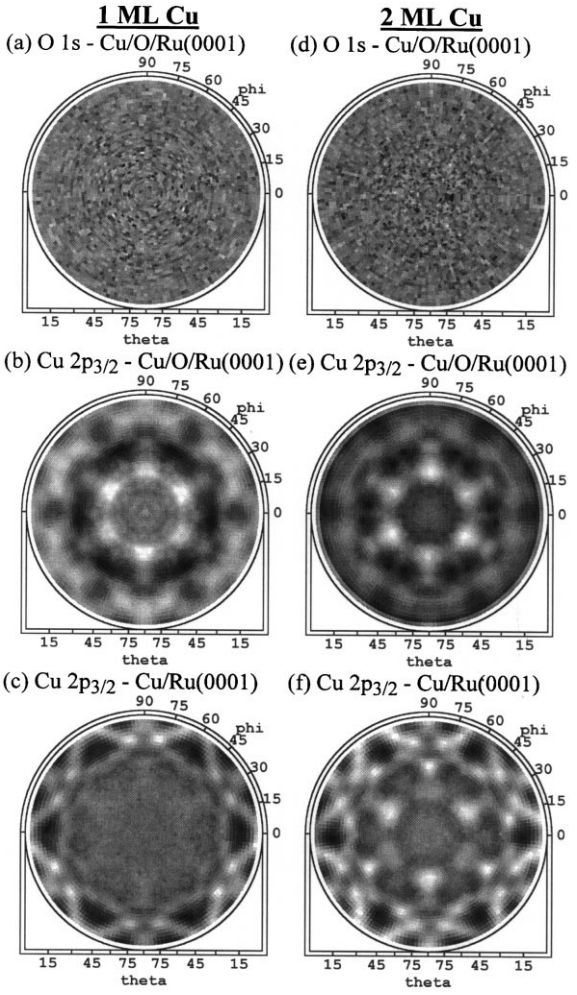

Fig. 18. Experimental XPD patterns from Cu/O/Ru(0001) at 1.1 and 2.2 ML Cu coverages. (a) O 1s emission at 1.1 ML Cu coverage. (b) Cu $2p_{3/2}$ emission at 1.1 ML Cu coverage. (c) Comparison to Cu $2p_{3/2}$ emission at 1.1 ML Cu coverage on clean Ru(0001). (d) O 1s emission at 2.2 ML Cu coverage. (e) Cu $2p_{3/2}$ emission at 2.2 ML Cu coverage. (f) Comparison to Cu $2p_{3/2}$ emission at 2.0 ML Cu coverage on clean Ru(0001).

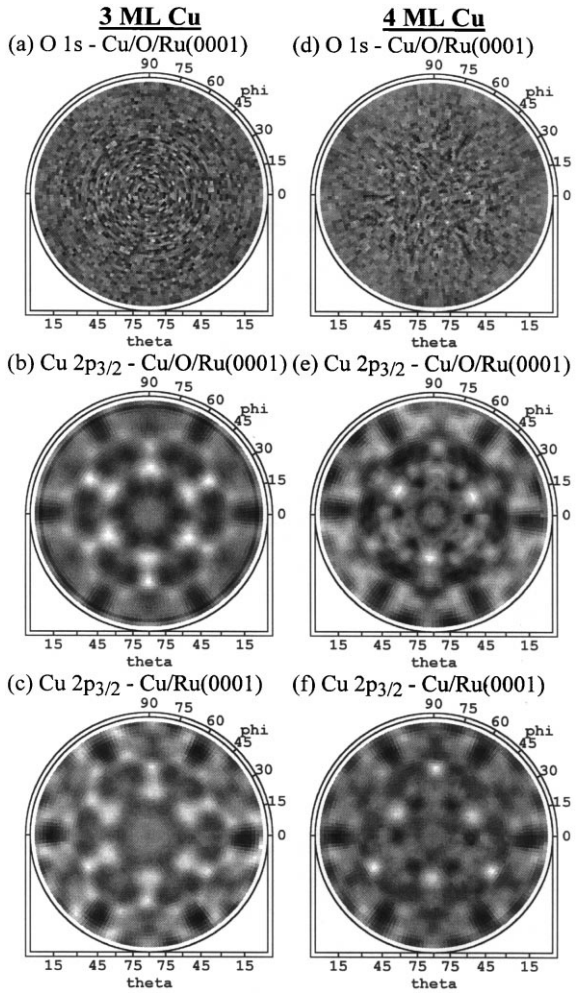

Fig. 19. Experimental XPD patterns from Cu/O/Ru(0001) at 3.2 and 3.7 ML Cu coverages. (a) O 1s emission at 3.2 ML Cu coverage. (b) Cu $2p_{3/2}$ emission at 3.2 ML Cu coverage. (c) Comparison to Cu $2p_{3/2}$ emission at 2.9 ML Cu coverage on clean Ru(0001). (d) O 1s emission at 3.7 ML Cu coverage. (e) Cu $2p_{3/2}$ emission at 3.7 ML Cu coverage. (f) Comparison to Cu $2p_{3/2}$ emission at 4.2 ML Cu coverage on clean Ru(0001).

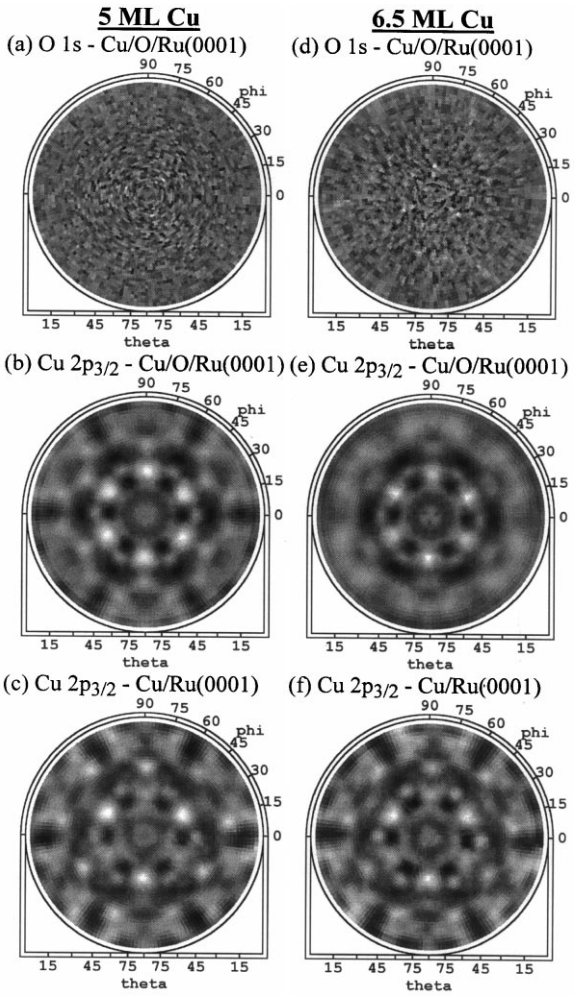

Fig. 20. Experimental XPD patterns from Cu/O/Ru(0001) at 4.8 and 6.5 ML Cu coverages. (a) O 1s emission at 4.8 ML Cu coverage. (b) Cu $2p_{3/2}$ emission at 4.8 ML Cu coverage. (c) Comparison to Cu $2p_{3/2}$ emission at 4.9 ML Cu coverage on clean Ru(0001). (d) O 1s emission at 6.5 ML Cu coverage. (e) Cu $2p_{3/2}$ emission at 6.5 ML Cu coverage. (f) Comparison to Cu $2p_{3/2}$ emission at 6.5 ML Cu coverage on clean Ru(0001).

Cu $2p_{3/2}$ peak for Cu coverages on O/Ru(0001) of 1 and 2 ML, respectively. The comparison to the case of Cu grown on clean Ru(0001) is shown in Fig. 18c and f. The O 1s XPD patterns shown in Fig. 18a and d show no diffraction features whatsoever. Although the oxygen XPD patterns shown here have not been smoothed, as Fig. 17a was, no diffraction features are visible in these XPD patterns, even after considerable smoothing. The lack of any forward scattering peaks indicates that all of the oxygen floats on the Cu overlayer, and that none of the oxygen is subsurface or remains at the Cu/Ru interface, in disagreement with some prior conclusions concerning this system [19–21]. If any oxygen were subsurface for these two cases, there would be the possibility of forward scattering through overlying Cu or O atoms, with the Cu clearly being in an ordered structure, as seen in

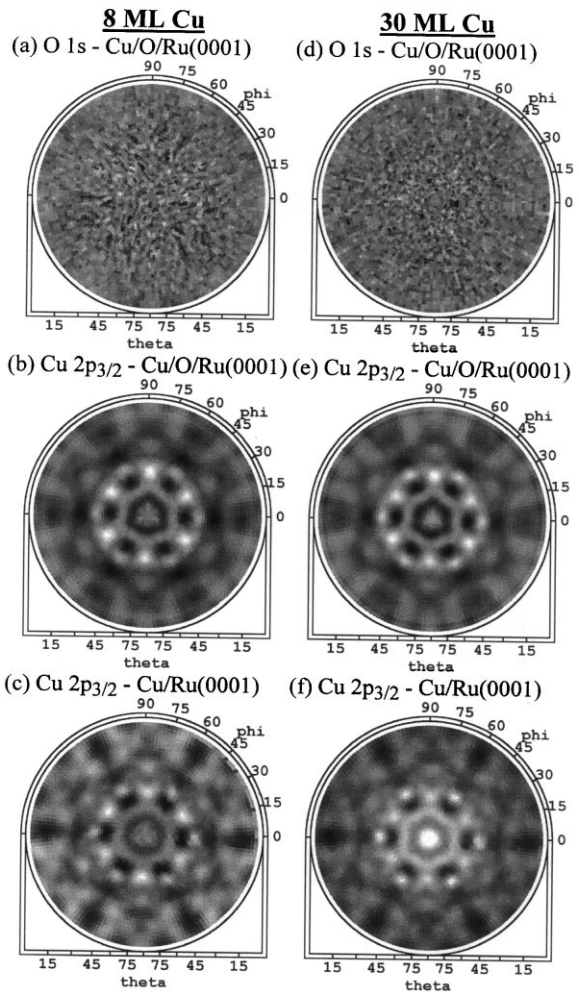

Fig. 21. Experimental XPD patterns from Cu/O/Ru(0001) at 8.0 and 30.5 ML Cu coverages. (a) O 1s emission at 8.0 ML Cu coverage. (b) Cu $2p_{3/2}$ emission at 8.0 ML Cu coverage. (c) Comparison to Cu $2p_{3/2}$ emission at 8.0 ML Cu coverage on clean Ru(0001). (d) O 1s emission at $\sim$30.5 ML Cu coverage. (e) Cu $2p_{3/2}$ emission at $\sim$30.5 ML Cu coverage. (f) Comparison to Cu $2p_{3/2}$ emission at $\sim$25.2 ML Cu coverage on clean Ru(0001).

the XPD patterns of Fig. 18b and e. This result is further verified by XPS coverage calculations, which indicate that the O coverage remains at $\sim$0.5 ML after Cu deposition, although due to noise in the O 1s signal as well as to errors in parameters used in our coverage calculations, the error in the O coverage determination may be as high as $\pm$0.05 ML [13]. The further lack of any features at even low θ confirms the results of LEIS studies [22] that the oxygen overlayer is disordered and/or perhaps highly mobile as a sort of lattice gas on the Cu surface. This is in contrast to the features seen in the XPD pattern shown in Fig. 18a for the ordered $p(2\times1)$-O/Ru(0001) structure. This result is not surprising, as several prior studies [60–62] have not reported an ordered oxygen structure on the Cu(111) surface. Consensus on the O/Cu(111) adsorption system, however, has not yet been reached, since ordered structures have also been reported [63–66]. Shown in Fig. 18b is the Cu $2p_{3/2}$ XPD pattern for a Cu coverage of 1 ML on the O-precovered Ru(0001) surface. A nearly six-fold pattern of high takeoff angle forward scattering peaks appears, indicating that there are atoms sitting in the three-fold hollow sites on top of the first layer before the first layer is complete, and that the two domain types are nearly equally occupied. This same six-fold pattern persists for 2 and 3 ML, as shown in Fig. 18e and Fig. 19b, and all three of these patterns look very much like the pattern for 3 ML Cu on clean Ru(0001), as shown in Fig. 19c. Thus, for Cu grown on O-precovered Ru in the 1–3 ML range, the growth appears to be initially via a Volmer–Weber (3D islands) mode rather than a Franck–Van der Merwe (layer-by-layer) mode. This is at first sight in disagreement with prior studies [19–22], which suggest layer-by-layer growth. For example, AES studies [19,22] suggested the layer-by-layer mode based on the agreement between the AES intensity ratio I_{Cu}/I_{Ru} as a function of coverage and a calculation based on the Gallon model [67] assuming layer-by-layer growth. Our findings are inconsistent with this AES study. Work-function oscillations seen during Cu growth [20,21] have also suggested surfactant-mediated layer-by-layer growth. However, these oscillations did not start until about 3 ML Cu coverage. Thus, our XPD results and the work-function measurements [20,21] can still be consistent with one another if the Cu initially grows as 3D islands, and then switches to layer-by-layer at thicker coverages above 3–4 ML. This type of growth has, for example, been seen by STM on the Co/Cu(100) system [68].

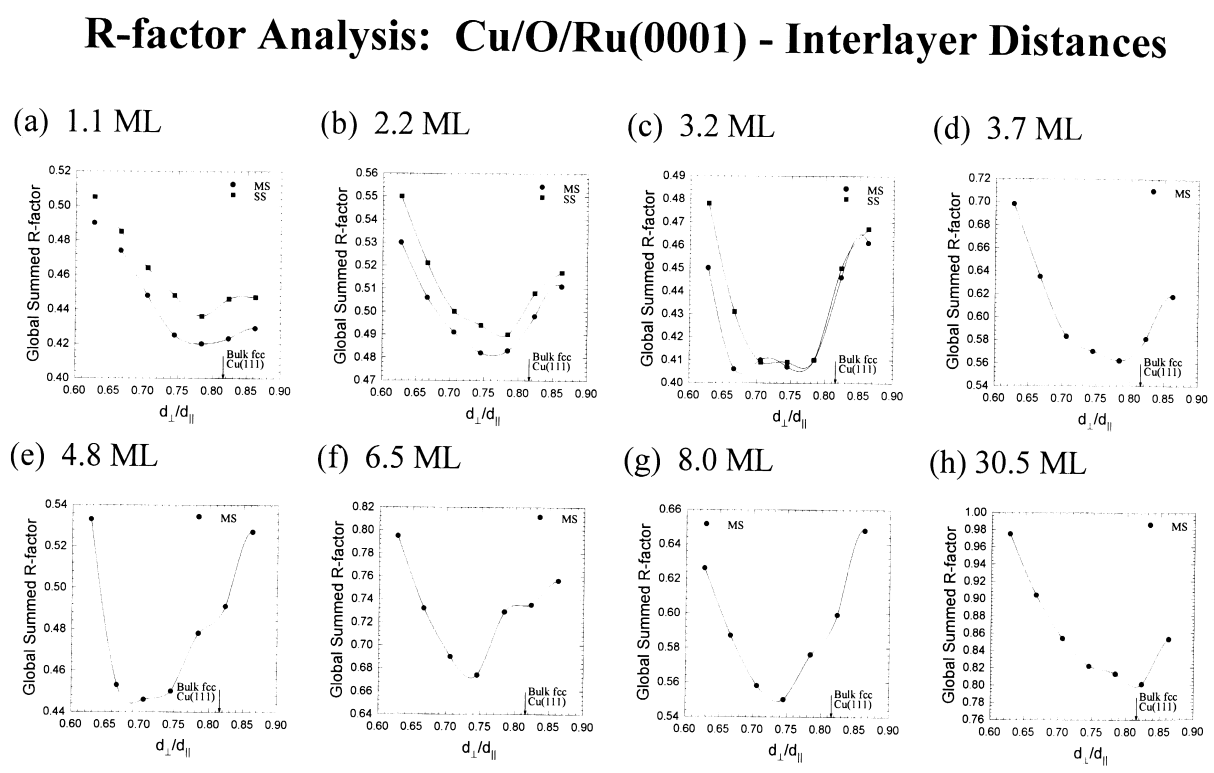

Fig. 22. Global *R*-factor plots comparing experiment to SSC calculations (for 1–3 ML) and MSC calculations (for all coverages) at various Cu coverages on O-precovered Ru(0001). (a) 1.1 ML, (b) 2.2 ML, (c) 3.2 ML, (d) 3.7 ML, (e) 4.8 ML, (f) 6.5 ML, (g) 8.0 ML, (h) 30.5 ML.

At thicker coverages ($\geq$40 ML), as shown in Fig. 19a and d, Fig. 20a and d and Fig. 21a and d, the XPD patterns for the O 1s peak again show absolutely no diffraction, again indicating that the oxygen floats on the Cu surface and is disordered and/or mobile. The XPS coverage determination also again yields essentially the same value of $\sim$0.5 ML as for the other Cu coverages [13], with no systematic variation in this coverage as the Cu thickness was increased. An interesting point to note at $\sim$4 ML coverage (obtained as noted previously after annealing to 325°C), is that a $(2\sqrt{3}\times 4\sqrt{3})$R30° LEED structure as reported in prior work was observed [20]. However, the oxygen XPD pattern still reveals no ordered structure. This is noteworthy in that it might be expected that oxygen could preferentially bind to sites in the $(2\sqrt{3}\times 4\sqrt{3})$R30° structure, in which case forward scattering features or diffraction rings could develop. In fact, the oxygen is still totally disordered and/or highly mobile. At $\sim$4 ML, the XPD pattern for the Cu $2p_{3/2}$ peak shown in Fig. 19e looks like the XPD patterns for 4 and 5 ML Cu on clean Ru(0001), as shown in Fig. 19f and Fig. 20c. At coverages of 5 ML and higher, shown in Fig. 20b and e and Fig. 21b and e, the Cu $2p_{3/2}$ XPD patterns look very much like the XPD patterns for 8 and 25 ML Cu on clean Ru(0001), as shown in Fig. 21c and f. For these higher coverages, the diffraction features at lower θ values are somewhat weaker and more smeared out with oxygen present, but this might be expected if growth is more multilayer and/or if there is diffuse scattering through the disordered oxygen overlayer. Thus, the structure is finally fcc Cu(111)-like with two domains, but the oxygen induces multilayer growth earlier than is the case of growth on clean Ru(0001). However, without

Table 3
Values of $d_\perp/d_\parallel$ for Cu/Ru(0001) and Cu/O/Ru(0001) as determined by *R*-factor comparison of experiment to SSC and MSC calculations; the SSC values are much less reliable for coverages of ≥ 4 ML, and are thus shown in parentheses

Cu coverage (ML)	$d_\perp/d_\parallel$			
	Cu/Ru(0001)		Cu/O-precovered Ru(0001)	
	SSC	MSC	SSC	MSC
1	–	–	0.783 ± 0.033	0.783 ± 0.033
2	0.733 ± 0.038	0.729 ± 0.034	0.761 ± 0.042	0.753 ± 0.042
3	0.740 ± 0.026	0.756 ± 0.018	0.737 ± 0.033	0.724 ± 0.039
4	(0.773 ± 0.022)	0.742 ± 0.016	(0.818 ± 0.032)	0.764 ± 0.033
5	(0.769 ± 0.047)	0.718 ± 0.018	(0.825 ± 0.013)	0.713 ± 0.028
6.5	(0.812 ± 0.026)	0.740 ± 0.014	(0.840 ± 0.020)	0.729 ± 0.020
8	(0.837 ± 0.016)	0.766 ± 0.018	(0.828 ± 0.021)	0.732 ± 0.026
≥ 25	(0.835 ± 0.014)	0.777 ± 0.020	(0.847 ± 0.027)	0.786 ± 0.032

a more detailed theoretical analysis, XPD does not allow us to determine whether the growth has become layer-by-layer at these thicker coverages. More studies of this system (e.g. with STM) may help to better understand the nature of the disorder in the oxygen overlayer, as well as the morphology of the surface at thicker Cu coverages with and without oxygen present.

We have also carried out an *R*-factor analysis of these O/Ru(0001) data so as to determine the ratio $d_\perp/d_\parallel$ for Cu coverages from 1 to 30 ML, and these curves as derived from MSC calculations are shown in Fig. 22a–h. Because of the greater uncertainty in the growth mode with oxygen present, it is more difficult to decide what thickness of cluster best represents this data. At 1 ML coverage, we have compared experiment to 2 ML MSC calculations since we believe that stacking occurs before the first monolayer is completed. For the other cases, we have used the nominal thickness of the overlayer up to 5 ML, and we have used 5 ML calculations for comparison to thicker coverages. All of the *R*-factors shown in Fig. 22 have been determined by comparing experiment to the same fcc Cu(111) clusters as used for Cu/Ru(0001). That is, we have not included the oxygen overlayer in our calculations since the oxygen overlayer is disordered, and therefore should have little effect on the Cu XPD pattern other than acting as an attenuating overlayer, with more serious effects for lower θ, as noted above. The results of the *R*-factor analysis for both Cu/Ru(0001) and Cu/O/Ru(0001) are shown in Table 3.

A plot of the change in interlayer contraction for Cu grown on O-precovered Ru(0001) is presented in Fig. 23a. These values do not significantly differ from those for Cu/Ru(0001), and thus the oxygen appears only to affect the growth and morphology rather than the short-range interplanar structure. Again, we also show here a theoretical estimate of $d_\perp/d_\parallel$ versus coverage based on 2D Frenkel–Kontorova calculations and a constant atomic-volume assumption. Shown in Fig. 23b is a plot of the symmetry (i.e. f_1) versus coverage for the Cu films grown on O-precovered Ru(0001). Here, with the exception of ~ 4 ML, which was a special case where the film was annealed, all of the symmetries are nearly six-fold. Thus it would seem that the presence of oxygen promotes the formation of two domains, or perhaps the six-fold symmetry is due to a greater amount of 3D character in the films, as was suggested earlier for Cu/Ru(0001). However, this conclusion would then be in disagreement with prior studies of this system [19–22].

4. Conclusions

This XPD analysis of the growth of Cu on clean and oxygen-precovered Ru(0001) permits several

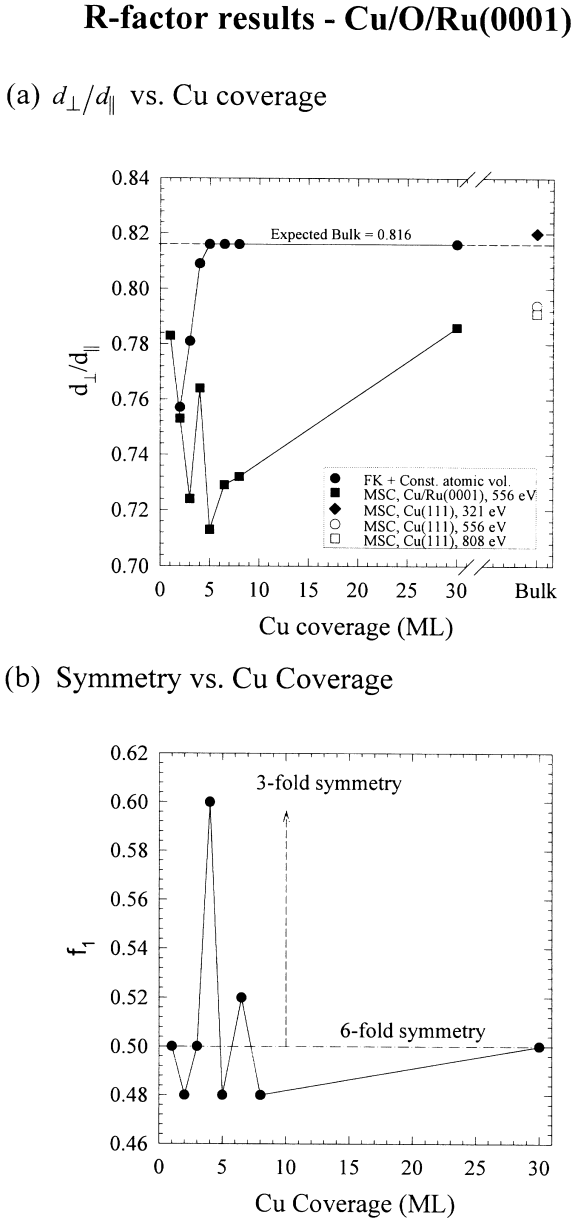

Fig. 23. As Fig. 14, but for oxygen-precovered Ru(0001). (a) Plot of $d_\perp/d_\parallel$=(Cu–Cu interplanar distance)/(Cu–Cu in-plane nearest-neighbor distance) versus coverage in monolayers (ML). ●, estimate of $d_\perp/d_\parallel$ using Cu areal densities derived from a 2D Frenkel–Kontorova model by Hamilton and Foiles [6] combined with a constant atomic-volume assumption. ■, $d_\perp/d_\parallel$ determined by *R*-factor comparisons between experimental XPD data from Cu/O/Ru(0001) and MSC calculations for Cu $2p_{3/2}$ emission at a photoelectron kinetic energy of 556 eV. ♦ and □, $d_\perp/d_\parallel$ determined by *R*-factor comparisons to experimental Cu $2p_{3/2}$ data obtained from Cu(111) by Naumović and Osterwalder at photoelectron kinetic energies of 321 and 808 eV, respectively [31]. ◦, $d_\perp/d_\parallel$ determined by an *R*-factor comparison between experimental Cu $2p_{3/2}$ XPD data obtained in our laboratory from a Cu(111) single crystal and MSC calculations at an energy of 556 eV. (b) Plot of the relative occupation of domain #1 versus coverage, with rotational symmetry indicated.

new structural conclusions as well as some general comments concerning the application of XPD to such epitaxial systems.

For Cu growth on clean Ru(0001), the first monolayer is pseudomorphic, and even at partial monolayer coverages forms in large islands $\geq$10–20 Å in diameter (the sensing limit of XPD) of the same structure. Our result of 2.15 Å for the distance between the Cu and the first Ru layer is consistent with prior experiments and theoretical studies of this first monolayer. For thicker overlayers, we have also shown that the short-range structure of Cu/Ru(0001) is fcc Cu(111), but with significant near-surface interlayer contraction for coverages between 2 and 8 ML. Comparison of experiment to MSC calculations suggests that the interlayer contraction may persist even up to 25 ML Cu coverage, although within the range of error, the results for this coverage are also consistent with our own *R*-factor comparison of MSC calculations to XPD patterns from a Cu(111) single crystal at photoelectron kinetic energies of 321, 556 and 808 eV (with 321 and 808 eV being measured by Naumović and Osterwalder), as well as with LEED results from Cu(111) single crystals. The Cu–Cu interlayer spacing shows a slower approach to the bulk fcc Cu(111) interlayer spacing than a simple theoretical estimate based on the 2D Frenkel–Kontorova model [6] and either a constant atomic volume assumption or a more complex analysis using elasticity theory. The appearance of sharp forward scattering peaks with distinct orientations and the excellent agreement with theory demonstrates that the misfit dislocation structures seen in STM [2–5] for 2–4 ML coverage actually thread through to the Cu–Ru interface. We have also shown that the SSC model predicts experiment reasonably well, but MSC

calculations do a better job of predicting the fine structure at low θ for lower coverages and at all θ for higher coverages. Thus, MSC calculations are important even at low coverages for a fully quantitative analysis of XPD data.

For Cu grown on O-precovered Ru(0001), we have shown that it initially forms 3D islands in the 1–3 ML range, and that all of the oxygen floats on the Cu overlayer and is highly disordered and/or mobile on the Cu surface. In addition, the presence of oxygen does not affect the interlayer contraction, but does affect the relative domain occupation of the Cu overlayer, leading to a dominance of six-fold character in the XPD patterns.

Finally, these results indicate that such XPD data, when combined with multiple scattering calculations and *R*-factor analysis, can yield quantitative information on such subtle issues as interlayer relaxations. Even the vertical position of a single monolayer for which no forward scattering features exist has been determined successfully. Our results also indicate that the calculated XPD patterns converge rather quickly with layer thickness, so that the experiment probes primarily the first five monolayers, and calculations can probably be truncated at about this level as well. We also have found that it is important to allow adequately for the various sources of broadening in the XPD features, and have used a Gaussian angular broadening as part of the optimization of the fit of theory to experiment. Without this additional broadening, theory in our case usually predicts sharper features than experiment, which can adversely affect the final *R*-factor comparisons leading to a structural conclusion. Lastly, even at XPS energies of ≥ 500 eV, a proper allowance for surface refraction in electron escape is important, and our data may suggest using a slightly higher effective inner potential than is usually estimated for the bulk (21–22 eV versus 14 eV). However, further investigation of this last point is needed to be more quantitative.

Acknowledgements

We thank Dr. A.P. Kaduwela for many insightful discussions of the theoretical modeling of photoelectron diffraction. We are also grateful to D. Naumovic and J. Osterwalder for providing us with XPD data for Cu(111) which appear in Fig. 15. This work has been supported by the Office of Naval Research under contracts N00014-90-5-1457 and N00014-94-1-0162, and by the Department of Energy, Basic Energy Sciences, Materials Sciences Division under contract DE-AC03-76SF00098.

References

[1] E. Bauer, Appl. Surf. Sci. 11/12 (1982) 479.
[2] G. Pötschke, J. Schröder, C. Günther, R.Q. Hwang, R.J. Behm, Surf. Sci. 252 (1991) 592.
[3] G.O. Pötschke, R.J. Behm, Phys. Rev. B 44 (1991) 1442.
[4] C. Günther, J. Vrijmoeth, R.Q. Hwang, R.J. Behm, Phys. Rev. Lett. 74 (1995) 754.
[5] C. Günther, PhD thesis, Universität Muenchen, 1994.
[6] J.C. Hamilton, S.M. Foiles, Phys. Rev. Lett. 75 (1995) 882.
[7] K. Christmann, G. Ertl, H. Shimizu, Thin Solid Films 57 (1979) 247.
[8] K. Christmann, G. Ertl, H. Shimizu, J. Catal. 61 (1980) 397.
[9] J.E. Houston, C.H.F. Peden, D.S. Blair, D.W. Goodman, Surf. Sci. 167 (1986) 427.
[10] J.E. Houston, C.H.F. Peden, Peter J. Feibelman, Phys. Rev. Lett. 56 (1986) 375.
[11] D.G. O'Neill, J.E. Houston, Phys. Rev. B 42 (1990) 2792.
[12] C. Park, E. Bauer, H. Poppa, Surf. Sci. 187 (1987) 86.
[13] S.D. Ruebush, PhD thesis, University of California–Davis, 1997.
[14] Ch. Ammer, K. Meinel, H. Wolter, A. Beckmann, H. Neddermeyer, Surf. Rev. Lett. 4 (1997) 1167.
[15] Ch. Ammer, K. Meinel, H. Wolter, H. Neddermeyer, Surf. Sci. 377 (1997) 81.
[16] S.D. Ruebush, R.E. Couch, S. Thevuthasan, Z. Wang, C.S. Fadley, Surf. Sci. 387 (1997) L1041.
[17] W.F. Egelhoff Jr.,, D.A. Steigerwald, J. Vac. Sci. Technol. A 7 (1989) 2167.
[18] A. Pavlovska, E. Fauer, Surf. Sci. 175 (1986) 369.
[19] K. Kalki, M. Schick, G. Ceballos, K. Wandelt, Thin Solid Films 228 (1993) 36.
[20] H. Wolter, M. Schmidt, K. Wandelt, Surf. Sci. 298 (1993) 173.
[21] M. Schmidt, H. Wolter, M. Nohlen, K. Wandelt, J. Vac. Sci. Technol. A 12 (1994) 1818.
[22] Y.G. Shen, D.J. O'Connor, H. van Zee, K. Wandelt, R.J. MacDonald, Thin Solid Films 263 (1995) 72.
[23] C.S. Fadley, Prog. Surf. Sci. 16 (1984) 275.
[24] C.S. Fadley, in: R.Z. Bachrach (Ed.), Synchrotron Radiation Research: Advances in Surface and Interface Science, Plenum, New York, 1992, pp. 421–517.

[25] C.S. Fadley, Surf. Sci. Rep. 19 (1993) 231.
[26] C.S. Fadley, J. Electron Spectrosc. 68 (1994) 19.
[27] J.J. Rehr, R.C. Albers, Phys. Rev. B 41 (1990) 8139.
[28] D.J. Friedman, C.S. Fadley, J. Electron Spectrosc. Relat. Phenom. 48 (1990) 689.
[29] A.P. Kaduwela, G.S. Herman, D.J. Friedman, C.S. Fadley, J.J. Rehr, Phys. Scripta 41 (1990) 948.
[30] A.P. Kaduwela, D.J. Friedman, C.S. Fadley, J. Electron Spectrosc. Relat. Phenom. 57 (1991) 223.
[31] Z. Wang, PhD thesis, University of California–Davis, 1997.
[32] D. Naumović, J. Osterwalder, private communication.
[33] D. Naumović, PhD thesis, Universität Fribourg, 1993.
[34] P. Dierckx, J. Comput. Appl. Math. 1 (1975) 165.
[35] L.F. Mattheis, Phys. Rev. 134 (1964) 970.
[36] L.F. Mattheis, in: David R. Linde (Ed.), CRC Handbook of Chemistry and Physics, 72nd ed., CRC Press, Boca Raton, FL, 1991–1992. Mattheis determined the Fermi energy (E_F) of copper to be 9.5 eV from band-structure calculations. Tables of work functions (ϕ) are available in the CRC Handbook, and for Cu(111), $\phi = 4.94$ eV. The inner potential is then $V_0 = E_F + \phi = 14.44$ eV.
[37] Y. Chen, A. Chassé, J. Garcia, M.A. Van Hove, C.S. Fadley, private communication.
[38] J.B. Pendry, private communication.
[39] M.P. Seah, W.A. Dench, Surf. Interface Anal. 1 (1979) 2.
[40] C.J. Powell, A. Jablonski, S. Tanuma, D.R. Penn, J. Electron Spectrosc. 68 (1994) 605.
[41] A.P. Kaduwela, PhD thesis, University of Hawaii, 1991.
[42] R.J. Baird, PhD thesis, University of Hawaii, 1977.
[43] M.A. Van Hove, S.Y. Tong, M.H. Elconin, Surf. Sci. 64 (1977) 85.
[44] R.S. Saiki, A.P. Kaduwela, M. Sagurton, J. Osterwalder, D.J. Friedman, C.S. Fadley, C.R. Brundle, Surf. Sci. 282 (1993) 33.
[45] P.M. Len, PhD thesis, University of California–Davis, 1997.
[46] S. Andersson, J.B. Pendry, Solid State Commun. 16 (1975) 563.
[47] M.A. Van Hove, W.H. Weinberg, C.-M. Chan, in: G. Ertl (Ed.), Low Energy Electron Diffraction: Experiment, Theory and Surface Structure Determination, vol. 6, Springer, Berlin, 1986, pp. 246–248.
[48] Y.G. Shen, D.J. O'Connor, J. Yao, H. van Zee, R.H. Roberts, R.J. MacDonald, K. Wandelt, J. Vac. Sci. Technol. A 13 (1995) 1478.
[49] P.J. Feibelman, J.E. Houston, H.L. Davis, D.G. O'Neill, Surf. Sci. 302 (1994) 81.
[50] S.D. Ruebush, R.X. Ynzunza, S. Thevuthasan, A.P. Kaduwela, M.A. Van Hove, C.S. Fadley, Surf. Sci. 328 (1995) 302.
[51] K. Baberschke, Appl. Phys. A 62 (1996) 417.
[52] S. Müller, B. Schulz, G. Kostka, M. Farle, K. Heinz, K. Baberschke, Surf. Sci. 364 (1996) 235.
[53] P.R. Watson, F.R. Shepard, D.C. Frost, K.A.R. Mitchell, Surf. Sci. 72 (1978) 562.
[54] S.P. Tear, K. Roll, M. Prutton, J. Phys. C 14 (1981) 3297.
[55] J. Neve, P. Westrin, J. Rundgren, J. Phys. C 16 (1983) 1291.
[56] I. Bartos, P. Jaros, A. Barbieri, M.A. van Hove, W.F. Chung, Q. Gai, M.S. Altman, Surf. Rev. Lett. 2 (1995) 477.
[57] T. Kraft, P.M. Marcus, Phys. Rev. B 48 (1993) 5886.
[58] P.M. Marcus, F. Jona, Surf. Rev. Lett. 1 (1994) 15.
[59] T.E. Madey, H.A. Engelhardt, D. Menzel, Surf. Sci. 48 (1975) 204.
[60] L.H. Dubois, Surf. Sci. 119 (1982) 399.
[61] H. Niehus, Surf. Sci. 130 (1983) 41.
[62] J. Haase, H.-J. Kuhr, Surf. Sci. 203 (1988) L695.
[63] G.W. Simmons, D.F. Mitchell, K.R. Lawless, Surf. Sci. 8 (1967) 130.
[64] J.H. Ho, R.W. Vook, J. Crystal Growth 44 (1978) 561.
[65] R.W. Judd, P. Hollins, J. Pritchard, Surf. Sci. 171 (1986) 643.
[66] F. Jensen, F. Besenbacher, E. Lægsgaard, I. Stensgaard, Surf. Sci. 259 (1991) L774.
[67] T.E. Gallon, Surf. Sci. 17 (1969) 486.
[68] C.M. Schneider, A.K. Schmid, P. Schuster, H.P. Oepen, J. Kirschner, in: R.F.C. Farrow et al. (Eds.), Magnetism and Structure in Systems of Reduced Dimensions, Plenum, New York, 1993, pp. 453–466.